Astronomy & Astrophysics

Gas versus dust sizes of protoplanetary discs: effects of dust evolution

L. Trapman[1], S. Facchini[2,3], M. R. Hogerheijde[1,4], E. F. van Dishoeck[1,2], and S. Bruderer[2]

[1] Leiden Observatory, Leiden University, Niels Bohrweg 2, 2333 CA Leiden, The Netherlands
  e-mail: `trapman@strw.leidenuniv.nl`
[2] Max-Planck-Institute für Extraterrestrische Physik, Giessenbachstraße, 85748 Garching, Germany
[3] European Southern Observatory, Karl-Schwarzschild-Str. 2, 85748 Garching bei München, Germany
[4] Anton Pannekoek Institute for Astronomy, University of Amsterdam, Science Park 904, 1090 GE Amsterdam, The Netherlands

ABSTRACT

Context. The extent of the gas in protoplanetary discs is observed to be universally larger than the extent of the dust. This is often attributed to radial drift and grain growth of the millimetre grains, but line optical depth produces a similar observational signature.
Aims. We investigate in which parts of the disc structure parameter space dust evolution and line optical depth are the dominant drivers of the observed gas and dust size difference.
Methods. Using the thermochemical model `DALI` with dust evolution included we ran a grid of models aimed at reproducing the observed gas and dust size dichotomy.
Results. The relation between R_{dust} and dust evolution is non-monotonic and depends on the disc structure. The quantity R_{gas} is directly related to the radius where the CO column density drops below 10^{15} cm^{-2} and CO becomes photodissociated; R_{gas} is not affected by dust evolution but scales with the total CO content of the disc. While these cases are rare in current observations, $R_{gas}/R_{dust} > 4$ is a clear sign of dust evolution and radial drift in discs. For discs with a smaller R_{gas}/R_{dust}, identifying dust evolution from R_{gas}/R_{dust} requires modelling the disc structure including the total CO content. To minimize the uncertainties due to observational factors requires FWHM$_{beam} < 1\times$ the characteristic radius and a peak S/N > 10 on the ^{12}CO emission moment zero map. For the dust outer radius to enclose most of the disc mass, it should be defined using a high fraction (90–95%) of the total flux. For the gas, any radius enclosing $>60\%$ of the ^{12}CO flux contains most of the disc mass.
Conclusions. To distinguish radial drift and grain growth from line optical depth effects based on size ratios requires discs to be observed at high enough angular resolution and the disc structure should to be modelled to account for the total CO content of the disc.

Key words. protoplanetary disks – astrochemistry – molecular processes – radiative transfer – line: formation – methods: numerical

1. Introduction

Observations of exoplanetary systems have revealed that they come in a large range of sizes, from multiple planets in the central ~0.3–1 AU of the system (e.g. TRAPPIST-1 or Kepler-90; Gillon et al. 2017; Cabrera et al. 2014) to systems with Jupiter mass planets in ~70 AU orbits around their host star (HR 8799; Marois et al. 2008). The diversity in planetary systems is linked to the diversity in protoplanetary discs from which these planets have formed.

To better understand this link, measurements of the properties of these discs are required. Of particular interest are the spatial extent of the gas, which sets the evolution of the disc, and the behaviour of the millimetre grains, which form the building blocks of the planets.

Observations have shown that the gas, traced by the ^{12}CO emission, extends further out than the millimetre grains traced by the (sub)millimetre continuum emission. Two physical processes contribute to the observed size dichotomy. The first is a difference in optical depth, with the line optical depth being much higher than the continuum optical depth (e.g. Dutrey et al. 1998; Guilloteau & Dutrey 1998; Facchini et al. 2017). Depending on how rapidly the density profile drops off in the outer disc, the optically thin continuum emission will drop below the detection

limit before the optically thick ^{12}CO emission. Based on the self-similar solution of viscous evolution, an exponentially tapered power law profile has been proposed to simultaneously fit the extent of the gas emission and the extent of the dust emission (e.g. Hughes et al. 2008; Andrews et al. 2009, see also Panić et al. 2008).

The second physical process setting the observed size dichotomy is grain growth and the subsequent inward radial drift of millimetre-sized grains. There is already extensive observational evidence that grains can grow to at least millimetre sizes (e.g. Testi et al. 2003; Natta et al. 2004; Lommen et al. 2007; Andrews & Williams 2005, 2007; Ricci et al. 2010). The large grains have decoupled from the gas. The gas is partly supported by a pressure gradient and therefore moves at slightly sub-Keplerian velocities. Gas drag causes the large grains, moving at Keplerian velocities, to slow down and move inwards. In addition, the maximum grain size seems to be decreasing as function of radial distance from the star, which is supported by both observations (e.g. Guilloteau et al. 2011; Pérez et al. 2012, 2015; Menu et al. 2014; Tazzari et al. 2016; Tripathi et al. 2018) and theoretical modelling results (e.g. Birnstiel et al. 2010, 2012).

Both radial drift and radially dependent grain growth cause the millimetre-sized grains to be confined in the inner regions of the disc, resulting in compact continuum emission at millimetre

wavelengths. Dust evolution also affects the CO chemistry and gas temperature and could therefore also change the observed gas disc size, determined from the ^{12}CO emission. Facchini et al. (2017) found that grain growth and settling results in colder gas with respect to the dust at intermediate disc heights, which reduces the CO excitation and emission.

The Atacama Large Millimeter/submillimeter Array (ALMA) is transforming our understanding of disc sizes. High resolution observations have shown that for several discs the dust outer edge drops off too sharply with radius and cannot be explained with the same exponential taper that reproduces the ^{12}CO emission (e.g. Andrews et al. 2011a, 2016; de Gregorio-Monsalvo et al. 2013; Piétu et al. 2014; Cleeves et al. 2016).

In addition, complete surveys of discs with ALMA have made it possible to study these disc properties not only for individual discs but also for the full disc population (e.g. Taurus: Andrews et al. 2013; Ward-Duong et al. 2018, Lupus: Ansdell et al. 2016, 2018, Chamaeleon I: Pascucci et al. 2016; Long et al. 2017, Upper Sco: Barenfeld et al. 2016, 2017, σ Ori: Ansdell et al. 2017, IC 348: Ruíz-Rodríguez et al. 2018). One of the main findings of these surveys is that most discs have very compact millimetre emission. For example, in the Lupus Survey (Ansdell et al. 2016, 2018) ~45% remain unresolved at ~20 AU radius resolution. It should be noted that the integration time used by these surveys is short, i.e. 1–2 min per source, resulting in a low signal-to-noise ratio (S/N) on the gas lines.

Observations show that the outer radius of the gas disc, traced by the ^{12}CO emission, is universally larger than the millimetre dust disc, as traced by the millimetre emission. Ansdell et al. (2018) measured gas and dust outer radii for 22 discs from the ^{12}CO 2–1 emission and 1.3 mm continuum emission. They found gas-dust size ratios R_{gas}/R_{dust} ranging from 1.5 to 3.5, with an average $\langle R_{gas}/R_{dust} \rangle = 1.96 \pm 0.04|_{\sigma_{obs}}$. Larger gas-dust ratios ($R_{gas}/R_{dust} > 4$) have been found for a few individual discs (e.g. Facchini et al. 2019). It should be noted that measurements of disc sizes are biased towards the most massive discs. Gas-dust sized differences for the faint end of the disc population are not well explored with current sensitivities and angular resolutions.

Both optical depth and radial drift contribute to the observed gas-dust size ratio. Quantitative comparison of how much these two effects affect the gas-dust size ratio has so far been limited to a single disc structure appropriate for the large and massive disc HD 163296 (Facchini et al. 2017).

In this paper, we expand the quantitative analysis of optical depth to a range of disc structures including dust growth and radial drift. In particular we focus on how disc mass, disc size, and dust evolution affect the gas-dust size difference. Additionally, we address what role observational factors such as resolution and sensitivity play in the observed gas-dust size difference. The set-up of the method and the models used in the paper are described in Sect. 2. The results are presented in Sect. 3. In Sect. 4 the connection between dust evolution and the dust outer radius is discussed. The conclusions are presented in Sect. 5.

2. Models

2.1. DALI with dust evolution

To study the effects of radial drift, grain growth, and optical depth on the gas-dust size dichotomy we use the thermo-chemical model DALI (Bruderer et al. 2012; Bruderer 2013) with dust evolution included by Facchini et al. (2017).

For a given physical structure, this version of DALI first calculates the radial dependence of the grain size distribution following the reconstruction routine from Birnstiel et al. (2015). This semi-analytical prescription provides a good representation of the more complete numerical models in Birnstiel et al. (2010). Birnstiel et al. (2015) divide the dust in the disc into two regimes: in the inner part of the disc, dust evolution is fragmentation dominated and the maximum grain size is set by the fragmentation barrier. In the outer disc, the maximum grain size is set by radial drift. The dust evolution is run for 1 Myr. Tests with models run for 10 Myr showed that the dust evolution timescale has only minimal effect on the dust outer radius (less than 17%).

Next, dust settling is calculated by solving the advection-diffusion equation in the vertical direction for each grain size bin at every radial point in the model. Opacities are calculated at each (r, z) point of the model using the resulting local grain size distribution.

It should be noted that the local gas-to-dust mass ratio (Δ_{gd}) in the models is kept fixed at $\Delta_{gd} = 100$, i.e. only the dust properties are changed.

The DALI thermo-chemical computation can be split into three consecutive steps: first the continuum radiative transfer equation is solved using the input stellar spectrum and the grain opacities calculated in the previous step. This is done using a 3D Monte Carlo method. Next the abundances of atomic and molecular species are calculated by solving the time dependent chemistry at each point in the model. In this step the local grain size distribution is taken into account when computing the dust surface area available for processes such as gas-grain collisions, H_2 formation rate, freeze-out, thermal and non-thermal desorption, and hydrogenation. Using a non-LTE formulation the excitation of levels of the atomic and molecular species are calculated and the resulting gas temperature is determined by balancing the heating and cooling processes. Both the chemistry and the excitation are temperature dependent. The calculation is therefore performed iteratively until a self-consistent solution is found. A more detailed description of DALI can be found in Appendix A of Bruderer (2013). The implementation of dust evolution in DALI is described in Facchini et al. (2017).

2.2. Model set-up

The gas surface density profile of the models is described by a tapered power law that is often used to describe protoplanetary discs (e.g. Hughes et al. 2008; Andrews et al. 2009, 2011b; Tazzari et al. 2017). This simple parametric structure is based on the assumption that the gas structure is set by viscous accretion, where $\nu \propto R^\gamma$ (Lynden-Bell & Pringle 1974; Hartmann et al. 1998), i.e.

$$\Sigma_{gas}(R) = \frac{M_{disc}(2 - \gamma)}{2\pi R_c^2} \left(\frac{R}{R_c} \right)^{-\gamma} \exp\left[-\left(\frac{R}{R_c} \right)^{2-\gamma} \right]. \tag{1}$$

In this case, R_c is the characteristic radius where the surface density profile transitions from a power law to an exponential taper.

Under the assumption of vertical isothermality and hydrostatic equilibrium the vertical structure is given by a Gaussian density distribution (Kenyon & Hartmann 1987)

$$\rho_{gas} = \frac{\Sigma_{gas}}{\sqrt{2\pi}Rh} \exp\left[-\frac{1}{2} \left(\frac{z}{Rh} \right)^2 \right], \tag{2}$$

where $h = h_c(R/R_c)^\psi$, ψ is the flaring power-law index and h_c is the disc opening angle at R_c.

2.3. Grid of models

Both the characteristic size R_c and the total disk mass M_{disk} are expected to affect the observed extent of the disk. A set of models was run varying both parameters: $R_c = 20, 50$ AU and $M_{disk} = 10^{-2}, 10^{-3}, 10^{-4}, 10^{-5} M_\odot$. No models with larger R_c were run as we aim to reproduce the bulk of disk population, most of which are found to be small. For each of these physical structures three models are run with $\alpha = 10^{-2}, 10^{-3}, 10^{-4}$. For reference, a model with the same (R_c, M_{disc}) is run using DALI without dust evolution (no drift). In this model the dust is split into two grain populations: small grains with sizes ranging between 50 Å and 1 μm and large grains with sizes between 1 μm and 1 mm. These large grains are restricted to a scale height of χh, where $\chi < 1$, simulating that these grains have settled towards the midplane. The mass ratio of the large to the small grains is given by f_{large}.

Standard volatile [C]/[H] = 1.35×10^{-4} and [O]/[H] = 2.88×10^{-4} are assumed in all models and the chemistry is evolved over a timescale of 1 Myr, which is a representative age for protoplanetary disks. For longer timescales, CO is converted into CH_4/C_2H_2, as shown in Bosman et al. (2018) (see also Schwarz et al. 2018; Dodson-Robinson et al. 2018). This results in a overall underabundance of volatile CO, which has been found in a number of disks (e.g. Favre et al. 2013; Kama et al. 2016a; Cleeves et al. 2016; McClure et al. 2016; Miotello et al. 2017). To investigate how such an underabundance in CO affects the observed gas disk size, a subset of models was run with a lower [C]/[H] and [O]/[H]. These models are discussed in Sect. 4.1.

T Tauri stars are expected to have excess UV radiation as a result of accretion onto the stellar surface. This UV radiation is added to the spectra as a blackbody with $T = 10\,000$ K, with a luminosity computed from the accretion rate assuming that the gravitational potential energy is released as radiation with 100% efficiency (see also Kama et al. 2016b).

For analysis, the disks are assumed to be face on (i = PA = $0°$). The effect of inclination is discussed in Appendix A and is found to be minimal for $i \leq 50°$. In total 32 models are run. Their parameters are found in Table 1.

2.4. Measuring the outer radius

To investigate the gas-dust size difference we have to measure the size of a disc from observations. A disc size metric that is often adopted for these purposes makes use of the cumulative intensity profile, i.e. the flux is measured in increasingly larger apertures. The outer radius (R_{90}) is defined as the radius that encloses 90% of the total flux (F_{tot}) of the disc

$$0.9 = \frac{2\pi}{F_{tot}} \int_0^{R_{90}} I_\nu(r')r'\,dr'. \tag{3}$$

This method has the advantage that it can be easily and homogeneously applied to a large number of discs, even if these discs show signs of substructure (see e.g. Tripathi et al. 2017; Ansdell et al. 2018; Andrews et al. 2018). In addition, the method can be applied to the short integration observations used in recent surveys, where the limited sensitivity hinders a more complex analysis.

It should be noted that the resulting outer radius is an observational outer radius. How well this observational radius is related to underlying physical size of the disc is examined in Sect. 4.3.

In this work, the gas outer radius is measured from the extent of the ^{12}CO 2–1 emission in the moment zero map

Table 1. DALI parameters of the physical model.

Parameter	Range
Chemistry	
Chemical age	1 Myr
[C]/[H]	1.35×10^{-4}
[O]/[H]	2.88×10^{-4}
Physical structure	
γ	1.0
ψ	0.1
h_c	0.1 rad
R_c	[20, 50] AU
M_{gas}	$[10^{-5}, 10^{-4},$ $10^{-3}, 10^{-2}] M_\odot$
Gas-to-dust ratio	100
Dust properties – no drift	
f_{large}	0.85
χ	0.2
Dust properties – dust evolution	
α_{turb}	$[10^{-2}, 10^{-3}, 10^{-4}]$
ρ_{gr}	2.5 g cm^{-3}
v_{frag}	10 m s^{-1}
Composition	standard ISM[1]
Stellar spectrum	
T_{eff}	4000 K + Accretion UV
L_*	0.5 $L_\odot$
Observational geometry	
i	$0°$
PA	$0°$
d	150 pc

References. [1]Weingartner & Draine (2001), see also Sect. 2.5 in Facchini et al. (2017).

and the dust outer radius is measured from the extent of the 1300 μm continuum emission. Gas outer radii measured using the ^{12}CO 3–2 emission differ from those measured using the ^{12}CO 2–1 by less than 10%. For comparison, gas outer radii measured instead from the ^{13}CO 2–1 emission are shown in Appendix B.

We note that the moment zero map is a velocity integrated intensity (in Jy beam^{-1} km s^{-1}). This puts additional weight at the centre of the disc, where the line widths are larger. It would be more comparable to the continuum emission to use the peak intensity map, defined as the peak intensity of the spectrum at each spatial point. In Appendix C we compare gas outer radii derived from the moment 0 and the peak intensity map and find them to be nearly identical.

3. Results

In this section we investigate how dust evolution shapes the continuum and line emission and how it affects the dust and gas outer radii. This effect is quantitatively compared to the influence of other disc parameters (M_{disc}, R_c) and observational factors (signal to noise, size of the beam).

3.1. Dust radial intensity profiles

Dust evolution changes the distribution of the grains responsible for the millimetre continuum emission, resulting in a different radial intensity profile. Through Eq. (3) the dust outer radius is
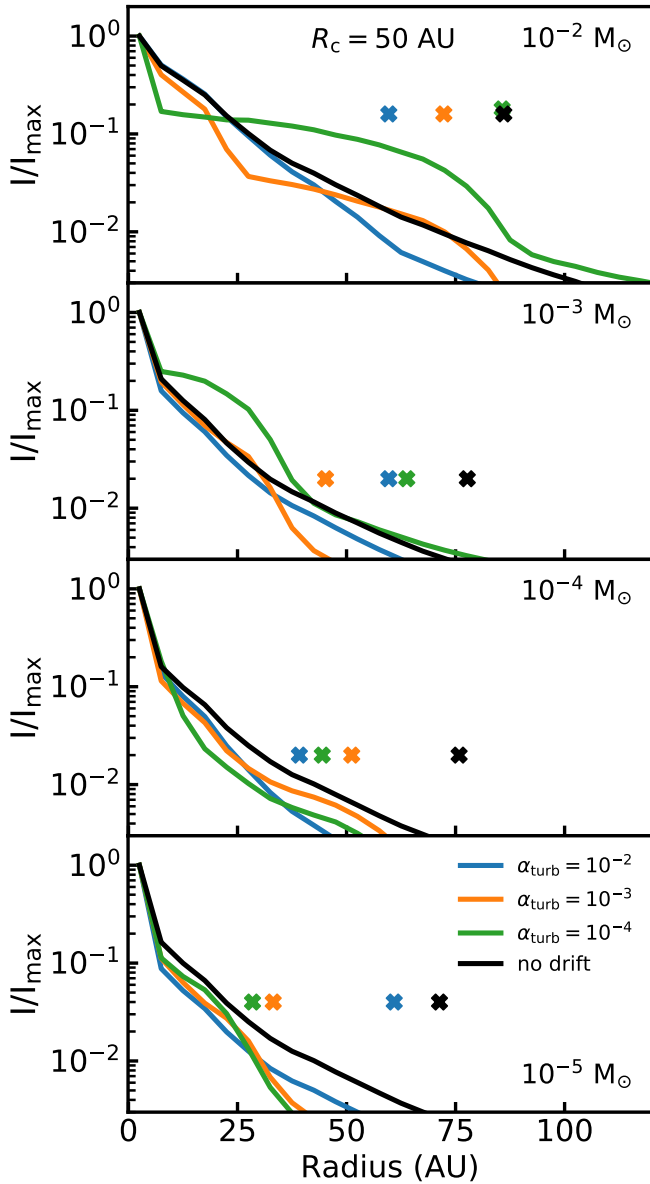
Fig. 1. Radial intensity profiles of the 1.3 mm continuum emission, normalised to the peak intensity, for the models with $R_c = 50$ AU. Crosses at an arbitrary height above the line denote the dust outer radii, defined as the radii enclosing 90% of the total flux. The resulting cumulative intensity curves are shown in Fig. E.1.

affected by the radial profile. In this section we investigate this link.

Figure 1 shows the normalised dust radial profiles of the models with $R_c = 50$ AU on a logarithmic intensity scale. The radial profiles of the models with $R_c = 20$ AU are shown in Fig. D.1. Starting with the lowest disc mass ($M_{disc} = 10^{-5}\ M_\odot$), all intensity profiles fall off steeply in the inner 10 AU. For discs with $\alpha_{turb} = 10^{-3}$–10^{-4} the intensity profile flattens between 10 to 25 AU and then steepens again. The dust outer radii of these two models are located at the second steepening off. For the model with $\alpha_{turb} = 10^{-2}$ and the so-called no drift model, the intensity profile is more extended and the dust outer radii of these models are larger.

For the discs with $M_{disc} = 10^{-4}\ M_\odot$ all intensity profiles of the dust evolution models are similar within 25 AU and their outer radii therefore lie close together. At higher disc mass

($M_{disc} \geq 10^{-3}\ M_\odot$) and low viscosity ($\alpha_{turb} \leq 10^{-3}$) a plateau of emission can be seen. The prominence of this plateau increases as α_{turb} decreases. For $M_{disc} = 10^{-2}\ M_\odot$ and $\alpha_{turb} = 10^{-4}$ about 75% of the emission is in the plateau and it has a large effect on the cumulative flux and the location of $R_{90,dust}$ (cf. Fig. E.1).

The emission plateau is directly linked to the presence of millimetre grains in the outer disc. When α_{turb} is low, the timescale for collisions that result in fragmentation is longer than the drift timescale and the size of the grains in the outer disc is set by radial drift (cf. Birnstiel et al. 2015). This causes a pile up of millimetre grains in the outer parts of the disc. Thus, the shape of the intensity profile is affected in a complex way by dust evolution.

3.2. ^{12}CO radial intensity profiles

The gas outer radius is measured from ^{12}CO 2–1 line emission, which is expected to be mostly optically thick throughout the disc. Dust evolution could affect the ^{12}CO emission by altering the temperature structure (Facchini et al. 2017).

In Fig. 2 the ^{12}CO 2–1 line emission profiles of the models with $R_c = 50$ AU are examined. Within each mass bin, the profiles are very similar in shape, suggesting that the effect of dust evolution on the ^{12}CO emission is neglible. The emission profiles drop off relatively slowly, which is expected for optically thick line emission that follows the temperature profile. At a certain radius the emission profile drops off steeply. In the model this radius corresponds to where the CO column (N_{CO}) density drops below 10^{15} cm^{-2}. Below a CO column density of $N_{CO} \leq 10^{15}$ cm^{-2}, CO is no longer able to effectively self-shield against photodissociation and is quickly removed from the gas phase (van Dishoeck & Black 1988). Defining the radius at which $N_{CO} = 10^{15}$ cm^{-2} as $R_{CO\ disk}$, this radius effectively encloses all of the CO emission and all of the volatile CO in the disc.

Using simple arguments, the observed gas outer radius $R_{90,gas}$ can be related analytically to $R_{CO\ disk}$. Assuming that the CO emission is optically thick ($I_{CO} \sim T_{gas}(R) \propto R^{-\beta}$) and that $R_{CO\ disk}$ encloses all ^{12}CO flux, we can write (full derivation can be found in Appendix F)

$$R_{90,gas} = 0.9^{\frac{1}{2-\beta}} R_{CO\ disk} = f^{\frac{1}{2-\beta}} R_{CO\ disk}, \qquad (4)$$

where f represents a more general case where the gas outer radius is defined using a flux fraction f.

Based on Eq. (4) the fraction of flux f used to define the gas outer radius should not affect the dependence of $R_{f,gas}$ on disc parameters such as M_{gas} or R_c. To highlight this point, Fig. 3 compares gas outer radii defined using 90 and 68% of the total flux. Independent of M_{gas}, R_c, and α_{turb} the models follow a tight linear relation that matches the expected relation $R_{68,gas} = 0.73 R_{90,gas}$, based on Eq. (4).

Summarising, the observational gas outer radius is directly related to the point of the disc where the CO column density reaches $N_{CO} = 10^{15}$ cm^{-2}. This relation is independent of the flux fraction used to define the gas outer radius.

3.3. Effect of dust evolution on $R_{90,dust}$ and $R_{90,gas}$

In the previous section dust evolution was shown to change the continuum intensity profile and the dust outer radius. Dust evolution also affects the CO chemistry (Facchini et al. 2017) and could therefore change the gas outer radius.

Figure 4 shows gas and dust outer radii as function of the turbulent α for different points in our (M_{disc}–R_c) parameter space.
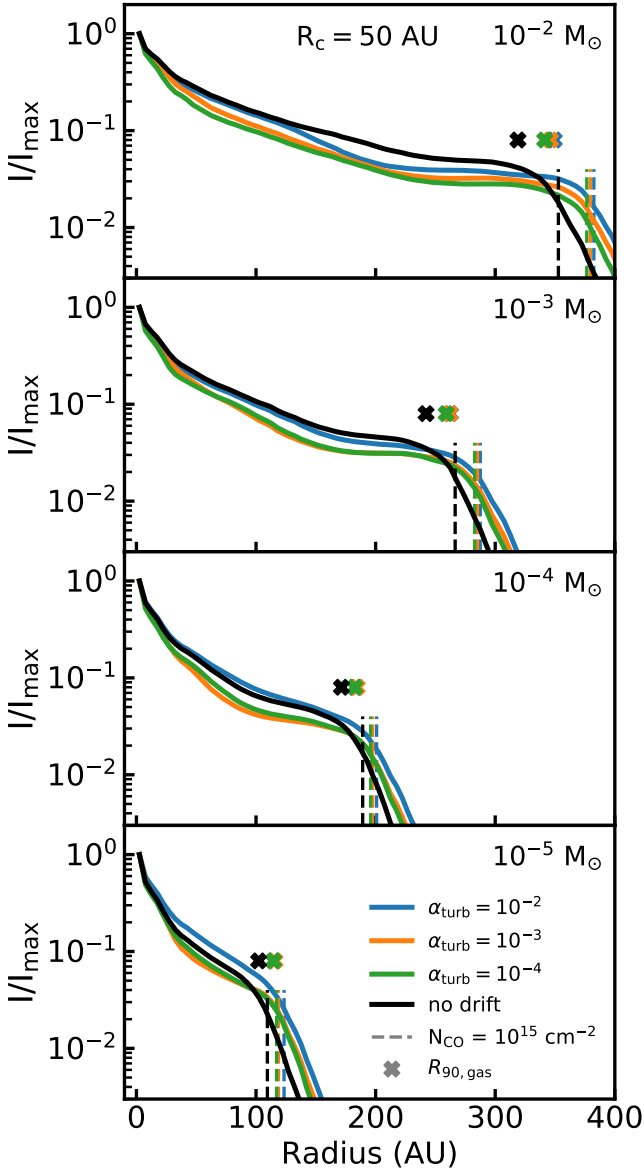
Fig. 2. Radial intensity profiles of the ^{12}CO 2–1 line emission, normalised to the peak intensity, for models with $R_c = 50$ AU. Crosses above the line denote the dust outer radii, defined as the radii enclosing 90% of the total flux. Vertical dashed lines denote the radius at which the CO column density drops below 10^{15} cm^{-2}, where it can be photodissociated effectively.
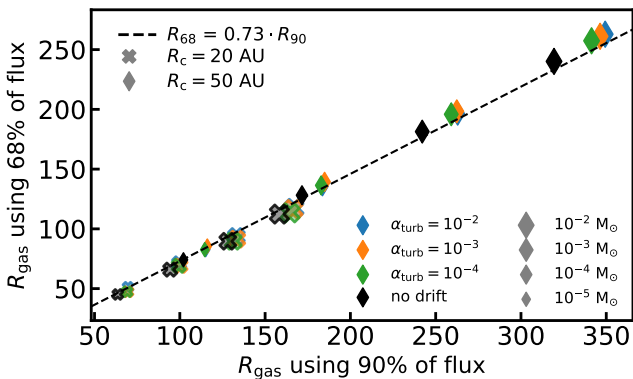

Fig. 3. Comparison between gas outer radii calculated using 90% of the flux and 68% of the flux. Dashed line shows the expected relation between these two observational outer radii based on Eq. (4).
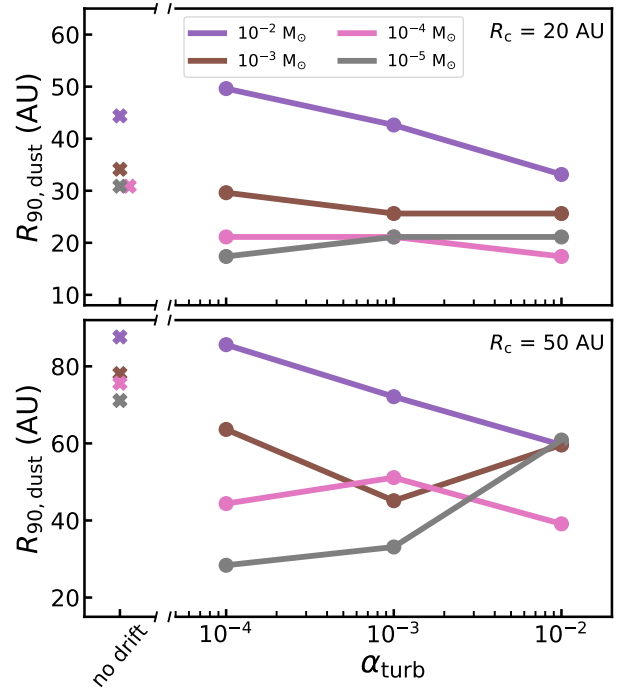
Fig. 4. For models with different (M_{disc}, R_c), $R_{90,dust}$ as function of α_{turb}. *Top panel*: models with $R_c = 20$ AU. *Bottom panel*: models with $R_c = 50$ AU. The crosses show the $R_{90,dust}$ for no drift model.

Compared to the no drift model, the dust radii of the dust evolution models are smaller up to a factor 1.5. No obvious trend of R_{dust} with α_{turb} is found. The dust outer radius scales with α_{visc} at high disc mass of 10^{-2} $M_\odot$, corresponding to a disc dust mass of 10^{-4} $M_\odot$. The trend is negative, with a higher α corresponding to a smaller $R_{90,dust}$. At high α fragmentation sets the maximum grain size throughout the disc, preventing millimetre grains from forming.

For lower disc masses the behaviour of $R_{90,dust}$ as function of α_{turb} depends on the characteristic size of the disc R_c. The intensity profile of discs with $R_c = 20$ AU is dominated by an inner core that is largely unaffected by α_{turb}. As a result $R_{90,dust}$ remains approximately constant with α_{turb}. For the larger discs ($R_c = 50$ AU) $R_{90,dust}$ varies with α_{turb}, but the trends are not monotonic for $M_{disc} = 10^{-3}$–10^{-4} $M_\odot$. For $M_{disc} = 10^{-5}$ the trend is monotonic again, but now $R_{90,dust}$ is larger for higher α_{turb}.

The effect of dust evolution on the gas outer radius is shown in Fig. 5. There are no noticeable changes in $R_{90,gas}$ when α_{turb} is varied, indicating that $R_{90,gas}$ is unaffected by dust evolution. The gas radii of the dust evolution models are larger than the gas radius of the no drift model.

A possible explanation is a difference in the amount of small grains in the outer disc. In the no drift model a fixed fraction of the dust is in small grains. In the dust evolution model the maximum grain size decreases with radius, representing the larger grains drifting inwards. However, in our model framework no mass is actually transferred inwards. As a result the amount of small grains in the outer disc is enhanced. These small grains can help shield the CO against photodissociation, allowing it to exist further out in the disc.

3.4. Effect of disc mass on $R_{90,gas}$ and $R_{90,dust}$

The observed gas-dust size difference is also affected by the difference in optical depth. The value $R_{90,dust}$ is calculated from the
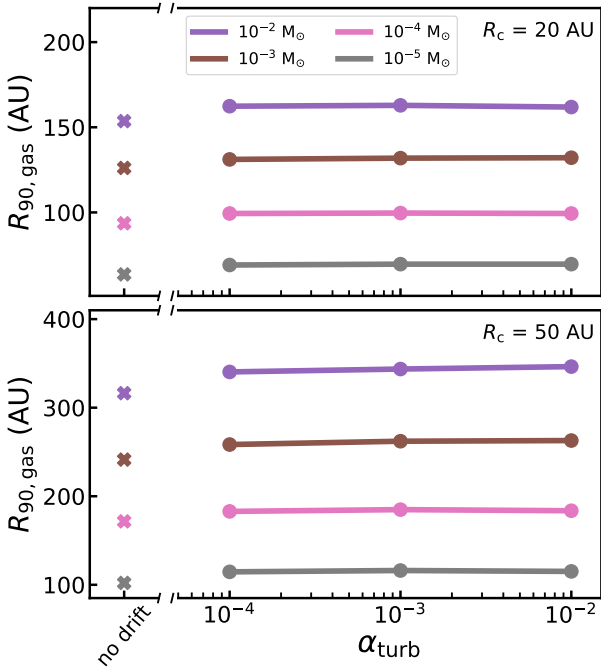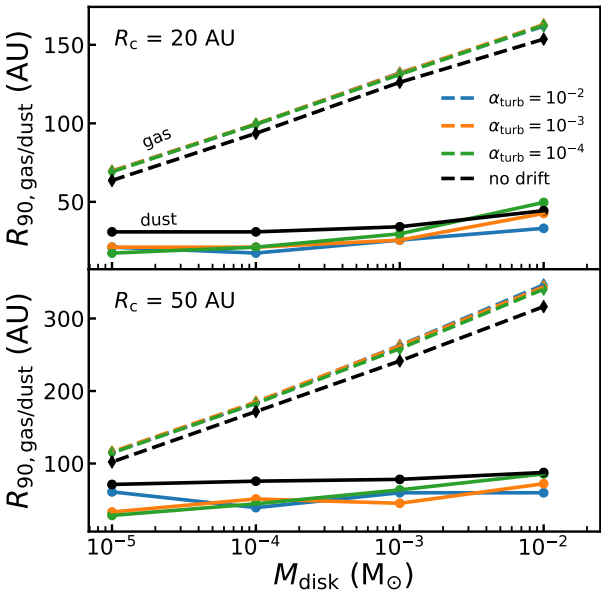
Fig. 5. For models with different $(M_{\rm disc}, R_{\rm c})$, $R_{\rm 90,gas}$ as function of $\alpha_{\rm turb}$. *Top panel*: models with $R_{\rm c} = 20$ AU. *Bottom panel*: models with $R_{\rm c} = 50$ AU. The crosses show the $R_{\rm 90,gas}$ for the no drift model.

Fig. 6. Disc outer radii vs. disc mass. *Top panel*: models with $R_{\rm c} = 20$ AU. *Bottom panel*: models with $R_{\rm c} = 50$ AU. Solid lines show dust outer radii. Dashed lines show gas outer radii.

millimetre continuum emission, that is mostly optically thin, whereas $R_{\rm 90,gas}$ is calculated from the optically thick ^{12}CO line emission. As optical depth is directly related to column density, the mass of the disc is also expected influence the observed outer radii.

Figure 6 shows $R_{\rm 90,gas}$ as function of $M_{\rm disc}$ for our standard model and models with different $\alpha_{\rm turb}$. The gas outer radii increase linearly with $\log_{10} M_{\rm disk}$, from $\sim 3 \times R_{\rm c}$ at $M_{\rm disc} = 10^{-5}$ $M_\odot$ up to $\sim 8 \times R_{\rm c}$ at $M_{\rm disc} = 10^{-2}$ $M_\odot$.

This relation can be understood qualitatively using the results from Sect. 3.2. Based on Eq. (4) and Fig. 6, we can write

$R_{\rm CO\ disk} \sim R_{\rm 90,gas} \propto \log_{10} M_{\rm disc}$. In the outer disc the column density scales as $N_{\rm CO} \sim \Sigma_{\rm gas} x_{\rm CO} \sim M_{\rm disc} \cdot x_{\rm CO} \cdot \exp(-R/R_{\rm c})$. At a radius $R_{\rm CO\ disk}$ the CO column density is known and the equation can be inverted to obtain $R_{\rm CO\ disk} \sim R_{\rm c} \log(M_{\rm disc} \cdot x_{\rm CO})$, similar to the relation found in Fig. 6.

It should be pointed that the dependence of $R_{\rm 90,gas}$ on $M_{\rm disc}$ is set by the shape of the density profile in the outer disc. In our models the density profile in the outer parts is described by an exponential, giving rise to the logarithmic dependence of $R_{\rm 90,gas}$ on $M_{\rm disc}$. If some process is affecting the density structure of the outer disc (e.g. due to tidal truncation or external photoevaporation; Facchini et al. 2016; Winter et al. 2018), the relation $R_{\rm 90,gas} \propto \log M_{\rm disc}$ no longer holds. Instead the relation between $R_{\rm 90,gas}$ and $M_{\rm disc}$ is set by the altered shape of the density structure in the region where $N_{\rm CO} = 10^{15}$ cm^{-2}.

The dust radii, shown as solid lines in Fig. 6, also increase with disc mass, but to a much smaller degree than the gas radii. Over the mass range considered in this work the dust radii increase by up to 1.5–$2 \times R_{\rm c}$. This is likely due to the millimetre continuum emission remaining optically thin throughout most of the disc. As the disc mass increases, the total continuum flux also increases, but the shape of the intensity profile and $R_{\rm 90,dust}$ derived from that profile remains largely unchanged. The small increase with dust mass can be attributed to a core of optically thick emission in the inner part of the disc. For higher disc masses this core increases in size which moves the 90% flux contour outwards. Overall we find that the effect of disc mass and optical depth on $R_{\rm 90,gas}$ is much larger than the effect of dust evolution on $R_{\rm 90,dust}$.

3.5. Dust evolution tracer: $R_{\rm 90,gas}/R_{\rm 90,dust}$

Combining the effects of dust evolution and disc mass (cf. Sects. 3.3 and 3.4), we now look at the gas-dust size dichotomy, quantified by $R_{\rm 90,gas}/R_{\rm 90,dust}$. Figure 7 shows $R_{\rm 90,gas}/R_{\rm 90,dust}$ as function of $M_{\rm disc}$. The fiducial no drift models show that $R_{\rm 90,gas}/R_{\rm 90,dust} = 1.5$–$3.5$, with a positive trend between $R_{\rm 90,gas}/R_{\rm 90,dust}$ and $M_{\rm disc}$. Comparing to Fig. 6 this trend is a direct result of $R_{\rm 90,gas}$ increasing with $M_{\rm disc}$.

The dust evolution models all lie above the no drift models, indicating that for a given disc mass a model that includes radial drift and grain growth has a larger $R_{\rm 90,gas}/R_{\rm 90,dust}$ than a model that only includes the effects of optical depth.

For the dust evolution models with $R_{\rm c} = 50$ AU, an overall positive trend of $R_{\rm 90,gas}/R_{\rm 90,dust}$ with disc mass is found, but the trend is not monotonic and depends on $\alpha_{\rm turb}$. For the smaller $R_{\rm c} = 20$ AU models the trend becomes negative towards higher disc masses.

From the trends in Fig. 7 it is clear that the size dichotomy $R_{\rm 90,gas}/R_{\rm 90,dust}$ can be used to identify dust evolution if the ratio is high enough ($R_{\rm 90,gas}/R_{\rm 90,dust} \geq 4$). Observationally, these cases are rare (see e.g. Facchini et al. 2019). For the majority of discs, a lower ratio is observed (cf. Ansdell et al. 2018). To identify dust evolution in these discs requires modelling of their ^{12}CO and dust emission, taking into account their total CO and dust content. The results also show that a direct determination of $\alpha_{\rm turb}$ from $R_{\rm 90,gas}/R_{\rm 90,dust}$ is not possible.

3.6. Observational factors affecting $R_{\rm 90,gas}/R_{\rm 90,dust}$

3.6.1. Effect of beam size

Observational factors such as the size of the beam and the background noise level are also able to influence the gas-dust size
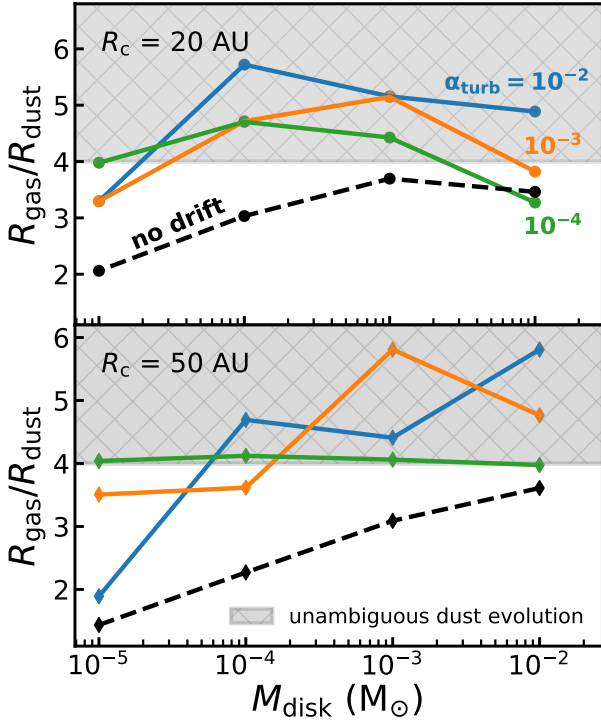
Fig. 7. Disc mass vs. $R_{90,gas}/R_{90,dust}$. *Top panel*: models with $R_c = 20$ AU. *Bottom panel*: models with $R_c = 50$ AU. Dashed lines show the no drift model, without dust evolution.
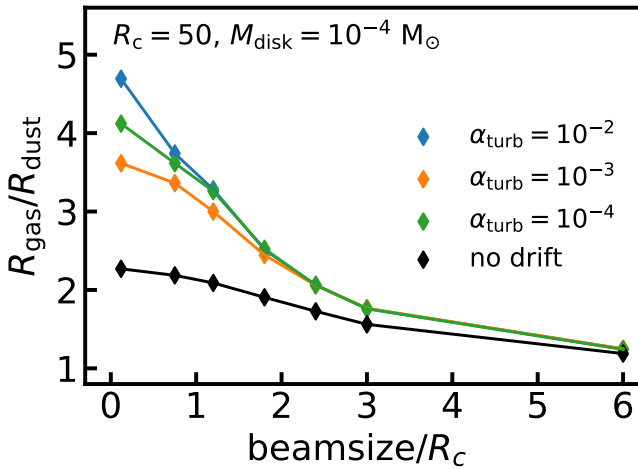

Fig. 8. Beam size vs. $R_{90,gas}/R_{90,dust}$. The effect of the beam scales with its relative size compared to the diameter of the disc. To highlight this, the beam size is expressed in terms of the characteristic size of the disc. Similar figures for various M_{disc} and R_c are shown in Fig. G.1.

dichotomy. Convolution with the beam smears out the intensity profile. For a centrally peaked intensity profile this moves R_{90} outwards. We use the full width at half maximum of the beam (FWHM$_{beam}$) as a measure of the beam size. For a beam size much larger than the observed disc the intrinsic differences between the gas and dust emission are washed out and $R_{90,gas}/R_{90,dust}$ is expected to approach unity.

Figure 8 shows the effect of beam size on $R_{90,gas}/R_{90,dust}$ for an example disc with $M_{disc} = 10^{-4}\ M_\odot$ and $R_c = 50$ AU. Similar panels for the other models are shown in Fig. G.1. The quantity $R_{90,gas}/R_{90,dust}$ decreases with beam size, approaching unity when the beam size becomes $\sim 3 \times R_c$. At a beam size $\sim 1 \times R_c$,
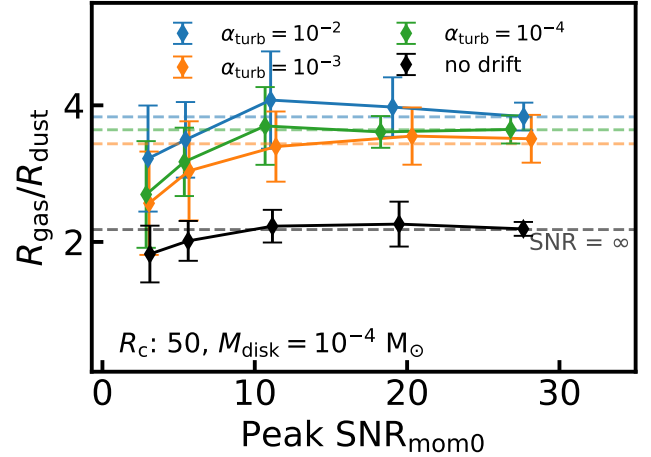
Fig. 9. Peak S/N in the moment 0 map of the ^{12}CO emission vs. $R_{90,gas}/R_{90,dust}$. Similar figures for various M_{disc} and R_c are shown in Fig. G.2. Peak S/N vs. $R_{90,gas}$ is shown in Fig. H.1.

$R_{90,gas}/R_{90,dust}$ has dropped below 4 and dust evolution can no longer be unambiguously be identified using only $R_{90,gas}/R_{90,dust}$ (see Sect. 3.5). However, if the uncertainties on $R_{90,gas}/R_{90,dust}$ are sufficiently small and the total CO content of the disc is known, dust evolution can still be inferred from observations with $FWHM_{beam} \leq 2R_c$.

3.6.2. Effect of noise level

Noise has two ways in which it can interact with the observational outer radius. Noise affects the shape of the curve of growth, thus changing the radius that encloses 90% of the total flux. In addition, the noise in the image sets the uncertainty on the total flux, which propagates through into the errors on R_{90}. For the gas-dust size difference, the noise on the gas emission is dominant. This is due to a difference in bandwidth: the gas emission is narrow in frequency, typically ~ 0.5km s^{-1}, whereas the continuum emission uses the full bandwidth of the observations. For example, a typical ALMA band 6 observation that has three continuum spectral windows (with a total bandwidth $\Delta\nu_{bandwidth} \simeq 2$ GHz) and 1 line spectral window centred on the ^{12}CO line (with line width $\Delta\nu_{line} \simeq 0.384$ MHz), the noise on the continuum is a factor $\sqrt{\Delta\nu_{bandwidth}/\Delta\nu_{line}} \sim 50$ lower compared to the line emission.

To simulate the effect of noise, empty channels taken from ALMA observations are added to the model image cube after convolution. The size of the convolution beam used for the model was matched to that of observations of Lupus discs (0.″25; Ansdell et al. 2018). The rms of the noise was scaled to obtain the requested peak S/N in the moment 0 map for the models.

The results are shown in Fig. 9 for the same example disc ($M_{disc} = 10^{-4}\ M_\odot$, $R_c = 50$ AU). The other discs are shown in Fig. G.2. The average $R_{90,gas}/R_{90,dust}$ measured at low S/N$_{mom0}$ is smaller than the noiseless case. As the S/N$_{mom0}$ increases it converges to the value measured in the absence of noise. A peak $S/N_{mom0} \sim 10$ is sufficient to recover the $R_{90,gas}/R_{90,dust}$ of the noiseless case. The uncertainties on $R_{90,gas}/R_{90,dust}$ are reduced when the peak S/N$_{mom0}$ increases, down to $\leq 10\%$ at a peak S/N_{mom0} of ~ 30. We note however that the noiseless $R_{90,gas}/R_{90,dust}$ is recovered within the error bars of the measured $R_{90,gas}/R_{90,dust}$ already at peak $S/N_{mom0} \sim 5$.

Summarising the effect of the observational factors, two recommendations for future observations can be made. Firstly,

differentiating between only optical depth and dust evolution in addition to optical depth requires $FWHM_{beam} \leq 1 \times R_c$. For a disc with $R_c = 20$ at 150 pc, this means a beam size of $0.''14 = 20$ AU. Secondly, to accurately measure the gas-dust size difference requires a peak $S/N \geq 10$ in the ^{12}CO moment zero. We note that an increased sensitivity will improve the uncertainty on the measured $R_{90,gas}/R_{90,dust}$ and can thus better distinguish cases where $R_{90,gas}/R_{90,dust}$ is unambiguously >4.

4. Discussion

4.1. CO underabundance and $R_{90,gas}$

In our models we have assumed standard interstellar medium (ISM) abundances for carbon and oxygen, resulting in an overall CO abundance of $x_{CO} \sim 10^{-4}$. However, recent observations have found CO to be underabundant by a factor 10–100 with respect to the ISM in several discs (e.g. Favre et al. 2013; Kama et al. 2016a; Cleeves et al. 2016; McClure et al. 2016). The low CO-based disc gas masses found by recent surveys suggest that CO could be underabundant in most discs (see e.g. Ansdell et al. 2016; Miotello et al. 2017; Long et al. 2017). As shown in Sect. 3.4 $R_{90,gas}$ is directly related to the CO content of the disc. The observed underabundance of CO in discs causes them to have a smaller observed gas disc size compared to our models.

To quantify the effect of CO underabundance on the measured $R_{90,gas}$ the models with $M_{disc} = 10^{-2} M_\odot$ were rerun, but now the total amount of carbon and oxygen in the disc is reduced by a factor $\delta_{C,O} = 0.1$–0.01, mimicking the observed underabundance of CO. Figure 10 shows that $R_{90,gas}$ decreases linearly with $\log_{10} \delta_{C,O}$, similar to the $R_{90,gas} \propto \log_{10} M_{disc}$ found earlier. This again highlights the importance of total CO content of the disc. As an example, let us consider two discs with the same total CO content. The first disc has a higher disk mass but is underabundant in CO $(M_{disc}, \delta_{C,O}) = (10^{-2} M_\odot, 0.1)$. The second disc is less massive but has standard ISM abundances $(M_{disc}, \delta_{C,O}) = (10^{-3} M_\odot, 1)$. For both discs we obtain the same $R_{90,gas}$, indicating that the gas outer radius depends on the total CO content of the disc.

A lower $R_{90,gas}$ also results in a lower $R_{90,gas}/R_{90,dust}$. Figure 11 shows $R_{90,gas}/R_{90,dust}$ as function of CO underabundance $\delta_{C,O}$. In the case of no CO underabundance ($\delta_{C,O} = 1$), $R_{90,gas}/R_{90,dust} = 2.5$–5.5. By decreasing the amount of CO in the disc by a factor of 100, the gas disc size decreases leading to $R_{90,gas}/R_{90,dust} = 1.5$ for the no drift model and $R_{90,gas}/R_{90,dust} = 2$–3.5 for the dust evolution models. We note that these values are for a disc with $M_{disk} = 10^{-2} M_\odot$. For a less massive disc that is also underabundant in CO $R_{90,gas}/R_{90,dust}$ is lower (cf. Sect. 3.4).

For a sample of 22 discs, Ansdell et al. (2018) measured $R_{90,gas}$ from the ^{12}CO 2–1 emission and $R_{90,dust}$ from the 1.3 mm continuum emission and found $R_{90,gas}/R_{90,dust} = 1.5$–3.5. The sample is skewed towards the most massive discs in their sample, where $M_{dust} = 0.5$–$2.7 \times 10^{-4} M_\odot$. This makes these massive discs comparable in dust content to the models discussed in this section ($M_{dust} = 10^{-4} M_\odot$). A simple, first order comparison between the models and the observations can therefore be made. CO underabundances of the discs in the Lupus sample are calculated by assuming a gas-to-dust mass ratio of 100 and comparing that to the ratio of $M_{CO\ based}/M_{dust}$, where $M_{CO\ based}$ is the CO-based gas mass estimate from Miotello et al. (2017). For example, a disc with $M_{CO\ based} = 10^{-3} M_\odot$ and $M_{dust} = 10^{-4} M_\odot$ is interpreted as having a CO underabundance of $\delta_{C,O} = \frac{M_{CO\ based}}{M_{dust}}/100 = 0.1$.
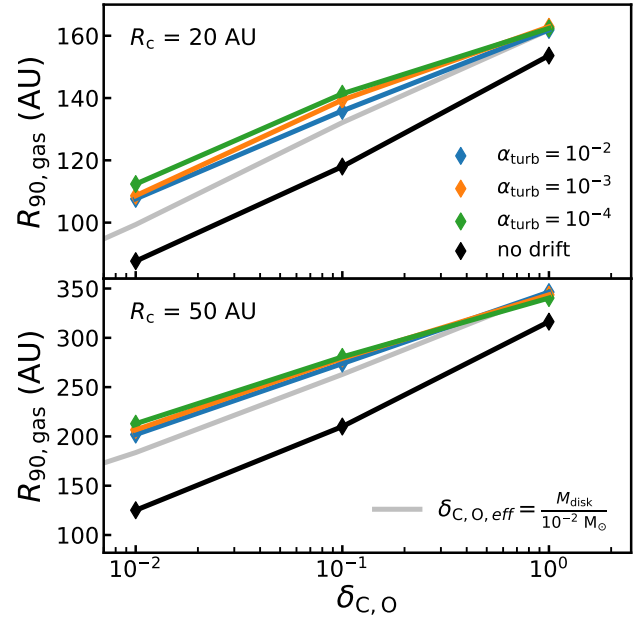
Fig. 10. Disc outer radii vs. CO underabundance. For comparison, the outer radii for the no drift model is shown in grey. *Top panel*: models with $R_c = 20$ AU. *Bottom panel*: models with $R_c = 50$ AU.
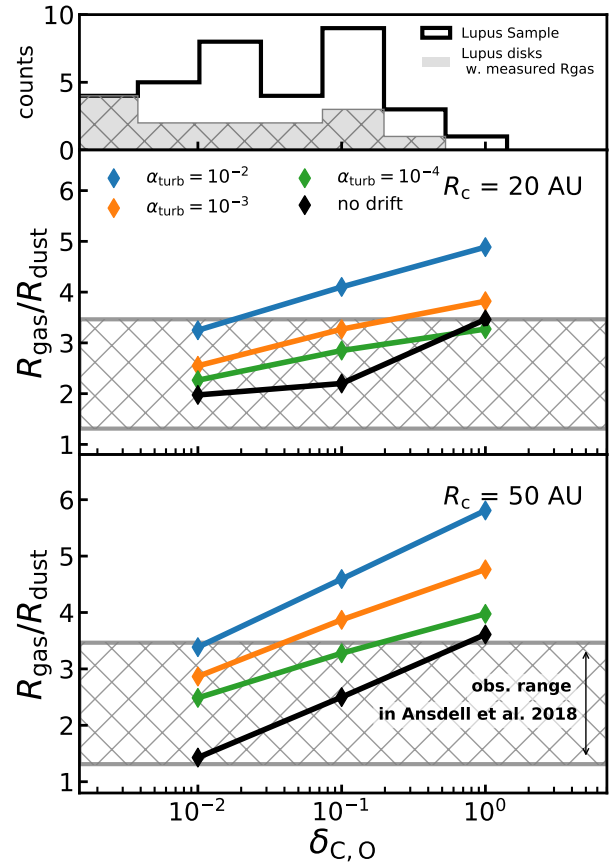

Fig. 11. CO underabundance vs. $R_{90,gas}/R_{90,dust}$. *Middle panel*: models with $R_c = 20$ AU. *Bottom panel*: models with $R_c = 50$ AU. The observed range of $R_{90,gas}/R_{90,dust}$ from Ansdell et al. (2018) is shown in grey. *Top panel*: histogram of the gas-to-dust ratios measured in Lupus (Ansdell et al. 2016; Miotello et al. 2017). These have been converted into an effective CO underabundance using $\delta_{C,O,eff} = \Delta_{gd}/100$, where Δ_{gd} is the gas-to-dust mass ratio.

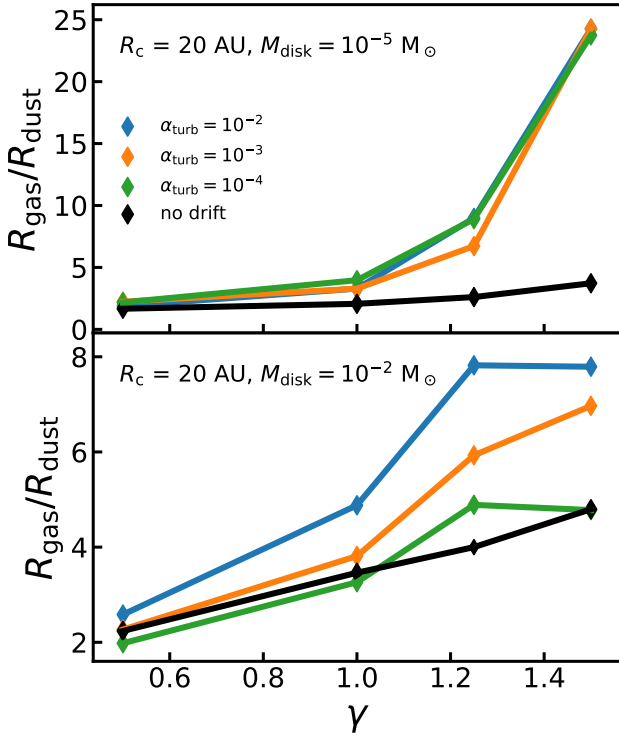**Fig. 12.** $R_{90,gas}/R_{90,dust}$ as function of the slope of the gas surface density. *Top panel*: models with $M_{disc} = 10^{-5} M_\odot$. *Bottom panel*: models with $M_{disc} = 10^{-2} M_\odot$.

Fig. 13. Fraction of flux f used to calculate R_{dust} and $R_{90,gas}$ compared to the fraction of M_{disc} within R_{dust} and $R_{90,gas}$. *Top panel*: dust emission; *bottom panel*: gas emission.

The calculated CO abundances show that several discs in the sample have $\delta_{C,O} \leq 10^{-2}$. For the same CO underabundance, the no drift model has $R_{90,gas}/R_{90,dust} = 1.5$–$2.0$, which is at the low end or below the observed range, suggesting that a least for some of the sources in the sample explaining the observed $R_{90,gas}/R_{90,dust}$ requires dust evolution. Modelling of the individual sources is required to provide a definitive identification of dust evolution, which is beyond the scope of this work (but see Trapman et al. 2018).

4.2. Effect of the surface density slope on outer radii

The surface density is governed by three parameters: R_c, M_{disc}, and γ (cf. Eq. (1)). The slope γ sets how the material is distributed in the disc and therefore affects the outer radius of the disc. In addition, the physical processes involved in dust evolution are also affected by γ. The slope of the gas surface density is not well constrained, having been observational constrained only for a few discs (e.g. Cleeves et al. 2016; Williams & McPartland 2016; Zhang et al. 2017; Miotello et al. 2018). Most of these studies find a value of $\gamma \sim 1.0$. In this section we investigate how much $R_{90,gas}/R_{90,dust}$ depends on γ. Figure 12 shows $R_{90,gas}/R_{90,dust}$ versus $\gamma = [0.5, 1.0, 1.5]$ for a set of low mass and high mass models. For low mass discs ($M_{disc} = 10^{-5} M_\odot$), $R_{90,gas}/R_{90,dust}$ increases drastically when γ is increased from 1.0 to 1.5 and has values of $R_{90,gas}/R_{90,dust} \simeq 24$ for models with dust evolution.

For the discs with dust evolution and $\gamma = 1.5$, millimetre-sized grains have been removed from the disc except for the inner few AU. As a result, the continuum emission is concentrated in this inner region and a very small dust outer radius is inferred. For the no drift model the dust radius is not similarly
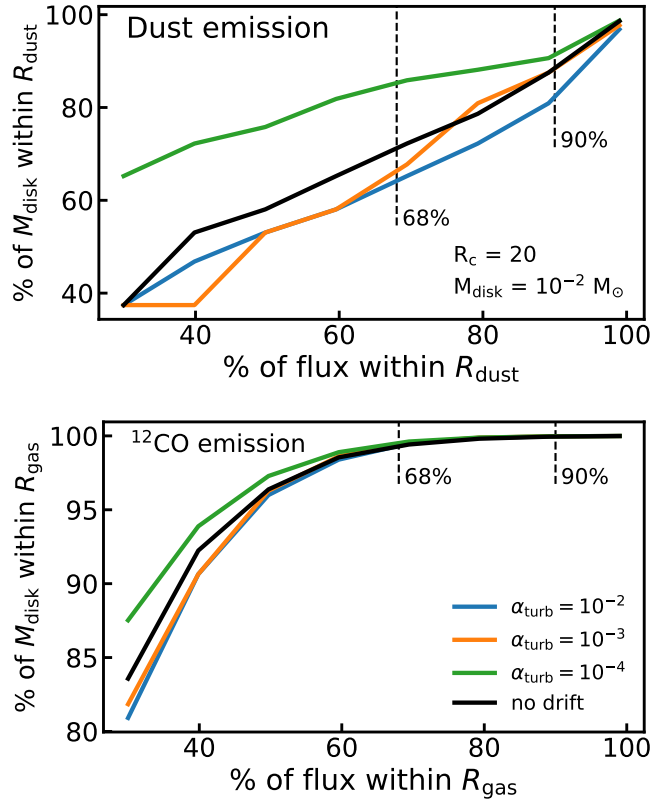
affected and the gas-dust size difference only increases to $R_{90,gas}/R_{90,dust} = 3.7$.

Increasing γ for the high mass disc does not have a significant effect on $R_{90,gas}/R_{90,dust}$. For the high mass disc the trends are similar for the no drift model and the dust evolution models. Here dust evolution is not significantly affected by the change in γ. For both low and high mass discs, decreasing γ from 1.0 to 0.5 results in a $R_{90,gas}/R_{90,dust}$ that is lower by a factor ~ 2.

4.3. Match of observed R_{out} to physical size of the disc

In this work we have quantified the radial extent of the disc using R_{90}, a flux based measure of the size of the disc. For this radius to be the outer edge of the disc in a physical sense, we could require that it encloses most (e.g. $\geq 90\%$) of the total mass of the disc.

In the cumulative intensity method used to define $R_{90,gas}$ and $R_{90,dust}$, a free parameter is the fraction of total flux f used (cf. Eq. (3)). In this work the outer radius is set at 90% of the total flux under the assumption that this radius encloses most of the disc. We investigate the requirement on f if we want the outer radius to enclose $\geq 90\%$ of the mass.

Figure 13 shows, for a given f used to compute $R_{90,gas}$ and $R_{90,dust}$, what fraction of the total disc mass is enclosed within this outer radius. Similar figures for the other discs in the model grid are shown in Appendix I.

For the dust emission, show in the top panel of Fig. 13, the fraction of enclosed disc mass (f_{mass}) correlates with the fraction of total flux (f_{flux}) used to define the outer radius. The relation between f_{mass} and f_{flux} is roughly linear, however the exact

trend depends on $\alpha_{\rm turb}$, $M_{\rm disc}$, and $R_{\rm c}$. Using a flux fraction of $f_{\rm flux} = 0.9$, between 75 and 90% of the total mass is enclosed with the exact fraction depending on $\alpha_{\rm turb}$. At $f_{\rm flux} = 0.68$ this has dropped to between 60 and 84% of the total mass.

The bottom panel of Fig. 13 shows that for the ^{12}CO emission, any gas outer radius $R_{90,\rm gas}$ defined using a fraction of total flux $f_{\rm flux} > 60\%$ encloses almost all (>98%) of the total disc mass and would thus meet our criterion of a physical outer radius (i.e. enclosing ≥90% of $M_{\rm disc}$). According to the definition of Eq. (3), these observational outer radii are not the same size. For example, a radius enclosing 90% of the flux has to be larger than a radius enclosing 75% of the flux. These observational outer radii are all related through Eq. (4) to the same physical point in the disc, where the CO column density equals 10^{15} cm^{-2} (cf. Sect. 3.2).

Summarising, the fraction of mass enclosed by $R_{\rm dust}$ scales roughly linearly with the fraction of continuum flux used to define $R_{\rm dust}$. To have the dust radius enclose most of the disc mass, the outer radius should be defined using a high fraction (90–95%) of the total flux. For the gas, any radius enclosing >60% of the flux contains most of the mass.

5. Conclusions

The gas in protoplanetary discs is found to be universally more extended than the dust. This effect can result from grain growth and subsequent inward drift of millimetre-sized grains. However, the difference in line optical depth between the optically thick ^{12}CO emission of the gas and the optically thin continuum emission of the dust also produces a gas-dust size dichotomy. In this work the thermochemical code DALI (Bruderer et al. 2012; Bruderer 2013), extended to include dust evolution (Facchini et al. 2017), is used to run a grid of models. Using these models, the impact of dust evolution, optical depth, and disc structure parameters on the observed gas-dust size difference are investigated. Our main conclusions can be summarised as follows:

– Including dust evolution leads to smaller observationally derived dust radii and larger gas radii. Dust evolution, as quantified by $\alpha_{\rm turb}$, has a complex effect on the dust radius, which also depends on the disc mass and the characteristic radius. The gas outer radius is unaffected by changes in $\alpha_{\rm turb}$.
– The gas outer radius $R_{90,\rm gas}$ is directly related to the radius at which the CO column density drops below 10^{15} cm^{-2} where CO becomes photodissociated. The value $R_{90,\rm gas}$ scales with the product $M_{\rm disc} \cdot x_{\rm CO}$, the total CO content of the disc; $R_{\rm gas}$ is directly related to the radius where ^{12}CO no longer is able to self-shield.
– The quantity $R_{90,\rm gas}/R_{90,\rm dust}$ increases with the total CO content and is higher for discs that include dust evolution. Discs with $R_{90,\rm gas}/R_{90,\rm dust} > 4$ are difficult to explain without dust evolution. For $R_{90,\rm gas}/R_{90,\rm dust} < 4$, deducing whether or not a disc is affected by dust evolution from the size ratio requires a measure of the total CO content. However, constraining $\alpha_{\rm turb}$ using $R_{90,\rm gas}/R_{90,\rm dust}$ is not possible.
– Increasing the beam size and lowering the peak S/N of the ^{12}CO moment 0 map both decrease the measured $R_{90,\rm gas}/R_{90,\rm dust}$. To minimize the effect of these observational factors requires $FWHM_{\rm beam} \le 1 \times R_{\rm c}$ and $S/N_{\rm peak,mom0} > 10$.
– $R_{90,\rm gas}/R_{90,\rm dust}$ increases with the slope of the surface density γ. In low mass discs with high γ, dust evolution removes almost all grains from the disc, resulting in large gas-dust size differences ($R_{90,\rm gas}/R_{90,\rm dust} \sim 24$).

– To have the dust radius enclose most of the disc mass, the outer radius should be defined using a high fraction (90–95%) of the total flux. For the gas, any radius enclosing >60% of the flux contains most of the mass.

The gas-dust size dichotomy is predominantly set by the structure and CO gas content of the disc, which can produce size differences up to $R_{90,\rm gas}/R_{90,\rm dust} \sim 4$. Discs with $R_{90,\rm gas}/R_{90,\rm dust} > 4$ can be directly identified as having undergone dust evolution, provided the gas and dust radii were measured with $FWHM_{\rm beam} \le 1 \times R_{\rm c}$. However, these discs are rare in current observations. For discs with a smaller gas-dust size difference, modelling of the disc structure including the total CO gas content is required to identify radial drift and grain growth.

References

Andrews, S. M., & Williams, J. P. 2005, AJ, 631, 1134
Andrews, S. M., & Williams, J. P. 2007, AJ, 671, 1800
Andrews, S. M., Wilner, D., Hughes, A., Qi, C., & Dullemond, C. 2009, AJ, 700, 1502
Andrews, S. M., Wilner, D. J., Hughes, A., et al. 2011a, ApJ, 744, 162
Andrews, S. M., Wilner, D. J., Espaillat, C., et al. 2011b, ApJ, 732, 42
Andrews, S. M., Rosenfeld, K. A., Kraus, A. L., & Wilner, D. J. 2013, ApJ, 771, 129
Andrews, S. M., Wilner, D. J., Zhu, Z., et al. 2016, ApJ, 820, L40
Andrews, S. M., Terrell, M., Tripathi, A., et al. 2018, ApJ, 865, 157
Ansdell, M., Williams, J. P., van der Marel, N., et al. 2016, ApJ, 828, 46
Ansdell, M., Williams, J. P., Manara, C. F., et al. 2017, AJ, 153, 240
Ansdell, M., Williams, J. P., Trapman, L., et al. 2018, ApJ, 859, 21
Barenfeld, S. A., Carpenter, J. M., Ricci, L., & Isella, A. 2016, ApJ, 827, 142
Barenfeld, S. A., Carpenter, J. M., Sargent, A. I., Isella, A., & Ricci, L. 2017, ApJ, 851, 85
Birnstiel, T., Ricci, L., Trotta, F., et al. 2010, A&A, 516, L14
Birnstiel, T., Klahr, H., & Ercolano, B. 2012, A&A, 539, A148
Birnstiel, T., Andrews, S. M., Pinilla, P., & Kama, M. 2015, ApJ, 813, L14
Bosman, A. D., Walsh, C., & van Dishoeck, E. F. 2018, A&A, 618, A182
Bruderer, S. 2013, A&A, 559, A46
Bruderer, S., van Dishoeck, E. F., Doty, S. D., & Herczeg, G. J. 2012, A&A, 541, A91
Cabrera, J., Csizmadia, S., Lehmann, H., et al. 2014, ApJ, 781, 18
Cleeves, L. I., Öberg, K. I., Wilner, D. J., et al. 2016, ApJ, 832, 110
de Gregorio-Monsalvo, I., Ménard, F., Dent, W., et al. 2013, A&A, 557, A133
Dodson-Robinson, S. E., Evans, II, N. J., Ramos, A., Yu, M., & Willacy, K. 2018, ApJ, 868, L37
Dutrey, A., Guilloteau, S., Prato, L., et al. 1998, A&A, 338, L63
Facchini, S., Clarke, C. J., & Bisbas, T. G. 2016, MNRAS, 457, 3593
Facchini, S., Birnstiel, T., Bruderer, S., & van Dishoeck, E. F. 2017, A&A, 605, A16
Facchini, S., van Dishoeck, E. F., Manara, C. F., et al. 2019, A&A, 626, L2
Favre, C., Cleeves, L. I., Bergin, E. A., Qi, C., & Blake, G. A. 2013, ApJ, 776, L38
Gillon, M., Triaud, A. H. M. J., Demory, B.-O., et al. 2017, Nature, 542, 456
Guilloteau, S., & Dutrey, A. 1998, A&A, 339, 467
Guilloteau, S., Dutrey, A., Piétu, V., & Boehler, Y. 2011, A&A, 529, A105
Hartmann, L., Calvet, N., Gullbring, E., & D'Alessio, P. 1998, ApJ, 495, 385
Hughes, A., Wilner, D., Qi, C., & Hogerheijde, M. 2008, ApJ, 678, 1119
Hunter, J. D. 2007, Comput. Sci. Eng., 9, 90
Kama, M., Bruderer, S., van Dishoeck, E. F., et al. 2016a, A&A, 592, A83
Kama, M., Bruderer, S., Carney, M., et al. 2016b, A&A, 588, A108
Kenyon, S. J., & Hartmann, L. 1987, ApJ, 323, 714
Lommen, D., Wright, C. M., Maddison, S. T., et al. 2007, A&A, 462, 211
Long, F., Herczeg, G. J., Pascucci, I., et al. 2017, ApJ, 844, 99
Lynden-Bell, D., & Pringle, J. E. 1974, MNRAS, 168, 603

Marois, C., Macintosh, B., Barman, T., et al. 2008, Science, 322, 1348

McClure, M. K., Bergin, E. A., Cleeves, L. I., et al. 2016, ApJ, 831, 167

Menu, J., Van Boekel, R., Henning, T., et al. 2014, A&A, 564, A93

Miotello, A., Bruderer, S., & van Dishoeck, E. F. 2014, A&A, 572, A96

Miotello, A., van Dishoeck, E., Williams, J., et al. 2017, A&A, 599, A113

Miotello, A., Facchini, S., van Dishoeck, E. F., & Bruderer, S. 2018, A&A, 619, A113

Natta, A., Testi, L., Neri, R., Shepherd, D. S., & Wilner, D. J. 2004, A&A, 416, 179

Panić, O., Hogerheijde, M. R., Wilner, D., & Qi, C. 2008, A&A, 491, 219

Pascucci, I., Testi, L., Herczeg, G., et al. 2016, ApJ, 831, 125

Pérez, L. M., Carpenter, J. M., Chandler, C. J., et al. 2012, ApJ, 760, L17

Pérez, L. M., Chandler, C. J., Isella, A., et al. 2015, ApJ, 813, 41

Piétu, V., Guilloteau, S., Di Folco, E., Dutrey, A., & Boehler, Y. 2014, A&A, 564, A95

Ricci, L., Testi, L., Natta, A., et al. 2010, A&A, 512, A15

Ruíz-Rodríguez, D., Cieza, L. A., Williams, J. P., et al. 2018, MNRAS, 478, 3674

Schwarz, K. R., Bergin, E. A., Cleeves, L. I., et al. 2018, ApJ, 856, 85

Tazzari, M., Testi, L., Ercolano, B., et al. 2016, A&A, 588, A53

Tazzari, M., Testi, L., Natta, A., et al. 2017, A&A, 606, A88

Testi, L., Natta, A., Shepherd, D. S., & Wilner, D. J. 2003, A&A, 403, 323

Trapman, L., Ansdell, M., Hogerheijde, M. R., et al. 2018, A&A, submitted

Tripathi, A., Andrews, S. M., Birnstiel, T., & Wilner, D. J. 2017, ApJ, 845, 44

Tripathi, A., Andrews, S. M., Birnstiel, T., et al. 2018, ApJ, 861, 64

van Dishoeck, E. F., & Black, J. H. 1988, ApJ, 334, 771

Ward-Duong, K., Patience, J., Bulger, J., et al. 2018, AJ, 155, 54

Weingartner, J. C., & Draine, B. 2001, ApJ, 548, 296

Williams, J. P., & McPartland, C. 2016, ApJ, 830, 32

Winter, A. J., Clarke, C. J., Rosotti, G., et al. 2018, MNRAS, 478, 2700

Zhang, K., Bergin, E. A., Blake, G. A., Cleeves, L. I., & Schwarz, K. R. 2017, Nat. Astron., 1, 0130

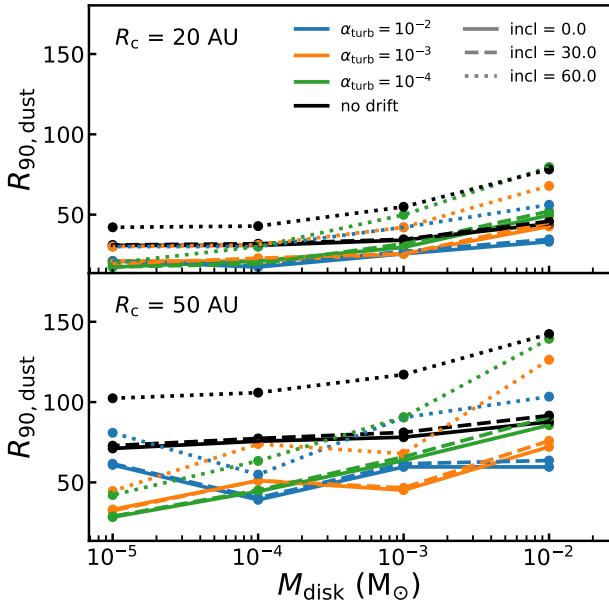## Appendix A: Effect of inclination

Fig. A.1. Effect of inclination on measuring the dust outer radius. Discs with a R_C = 20 AU and R_C = 50 AU are shown in the top and bottom panel, respectively.
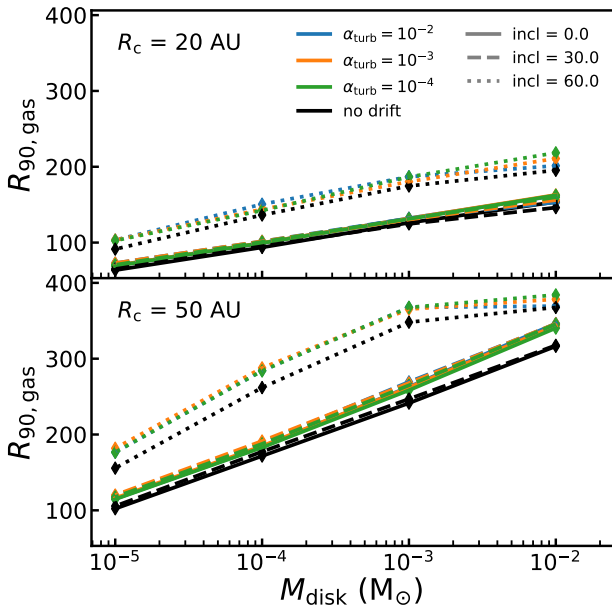

Fig. A.2. Effect of inclination on measuring the gas outer radius. Discs with a R_C = 20 AU and R_C = 50 AU are shown in the top and bottom panel, respectively.

In the analysis in this work all disc radii were measured from discs with an inclination of 0°. Inclination increases the optical depth along the line of sight. This can affect the measured size of the disc, especially for the gas, which is determined from optically thick emission (cf. Sect. 2.4).

Figures A.1 and A.2 show gas and dust radii measured from images with an inclination of $i = 0°, 30°, 60°$. For the inclined images, the cumulative flux is instead calculated using elliptical apertures to account for the projection. Between $i = 0°$ and $i = 30°$ there is no noticeable difference in the outer radii. For 60° outer radii have become slightly larger, but even at the most

extreme the effect is smaller than a 50% increase. Thus the effect of inclination should only be considered for discs with high inclination ($i > 60°$) when trying to identify dust evolution.

Appendix B: Measuring $R_{90,gas}$ from ^{13}CO 2–1 moment zero maps
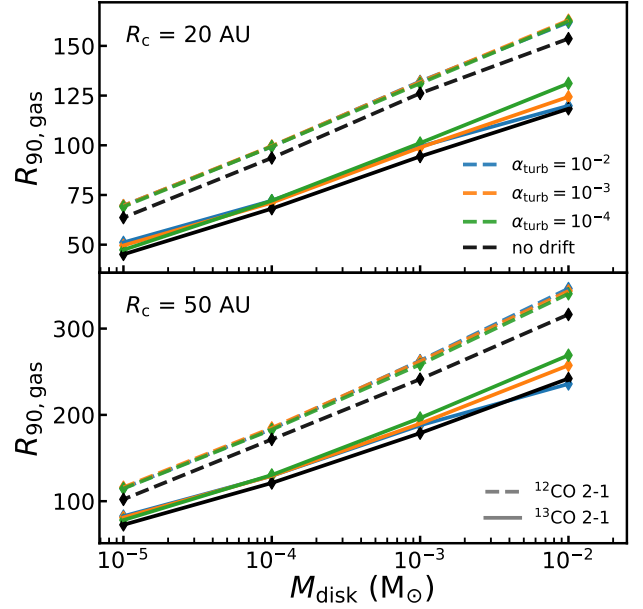
Fig. B.1. Comparison of gas outer radii measured from ^{13}CO 2–1 emission (solid lines) and ^{12}CO 2–1 emission (dashed lines).
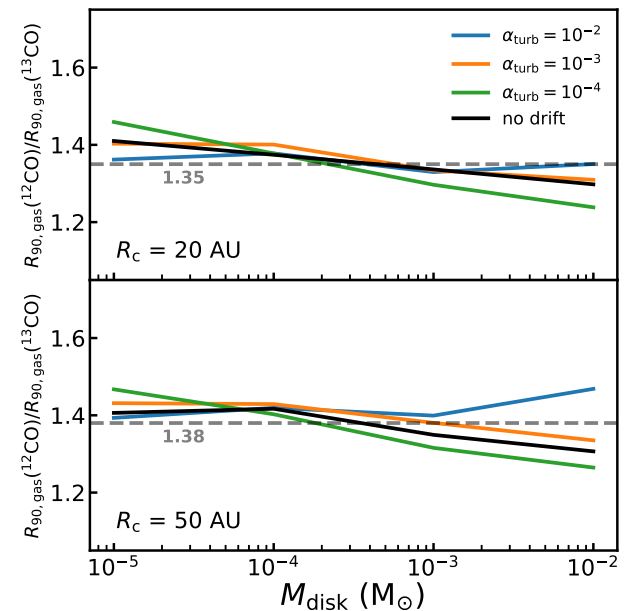
Fig. B.2. Ratio of gas outer radii measured from ^{12}CO 2–1 emission ($R_{90,gas}(^{12}CO)$) over ^{13}CO 2–1 emission ($R_{90,gas}(^{13}CO)$). The mean ratio of all models is shown in grey.

In this appendix, we investigate how the gas outer radius would differ, if instead it had been defined as the radius enclosing 90% of the ^{13}CO 3–2 flux. ^{13}CO is added to the model parametrically, by taking the CO abundances and scaling them with the ^{12}C/^{13}C elemental ratio, assumed to be ^{12}C/^{13}C = 77.

Figure B.1 shows $R_{90,gas}(^{13}CO)$ and $R_{90,gas}(^{12}CO)$ as function of disc mass. The value $R_{90,gas}(^{13}CO)$ also with disc mass in a similar manner to $R_{90,gas}(^{12}CO)$, i.e. $R_{90,gas}(^{13}CO) \sim \log_{10} M_{disk}$. As a result, using the ^{13}CO emission does not change the qualitative results seen in this work.

Figure B.2 shows the ratio $R_{90,gas}(^{12}CO)/R_{90,gas}(^{13}CO)$ for different disc masses. On average, $R_{90,gas}(^{12}CO)$ is 30–45% larger than $R_{90,gas}(^{13}CO)$ and has variations because α_{turb}, R_c, or M_{disc} are small. However we do not consider the effects of isotope-selective photodissociation, which become relevant in the outer part of the disc (cf. Miotello et al. 2014).

Appendix C: Measuring $R_{90,gas}$ from peak intensity maps
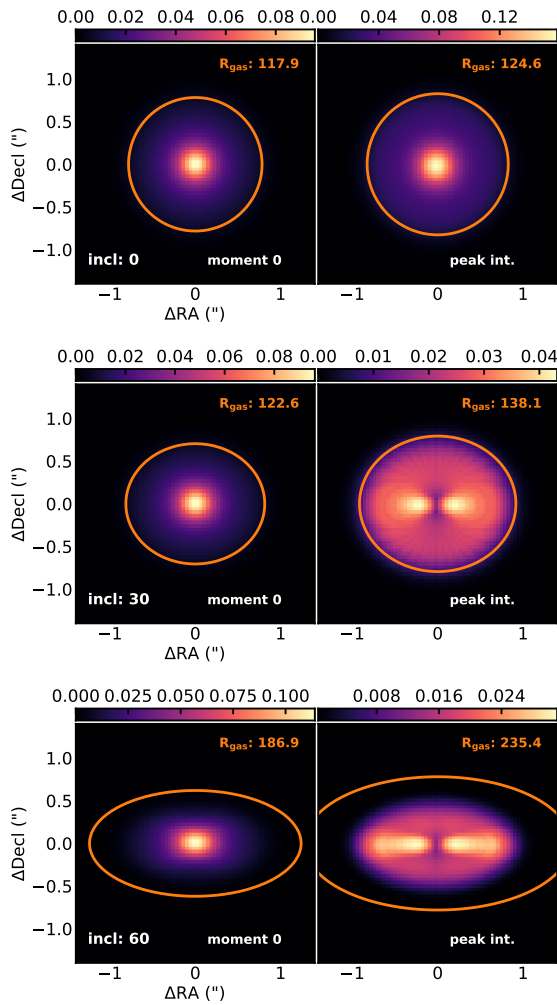
Fig. C.1. Comparison between outer radii derived from ^{12}CO moment 0 map (*left*) and the peak intensity (moment 8) map (*right*). The model shown has $M_{disc} = 10^{-3} M_\odot$, $R_c = 50$ AU, and $\alpha_{turb} = 10^{-4}$.

Fig. C.2. Gas radii measured from the peak intensity map vs. disc mass. *Top, middle, and bottom figures*: discs with inclinations of 0°, 30°, and 60°, respectively

The extent of the gas emission is measured from the moment zero map, which is constructed by integrating in spectral image cube over the frequency axis. As a result the gas emission has units (Jy beam^{-1} km s^{-1}). This method places extra emphasis on the inner part of the disc, where the Keplerian velocity structure of the gas produces the widest line profiles (in velocity).

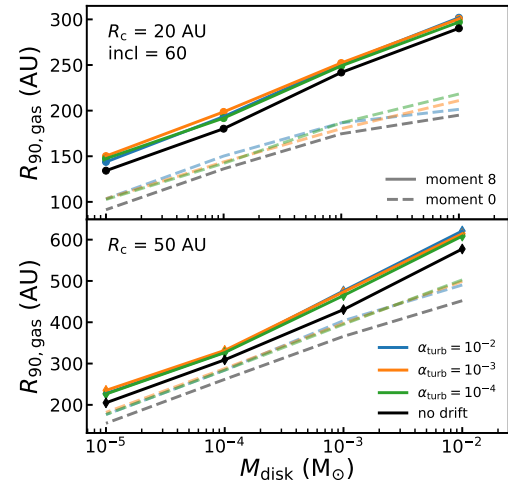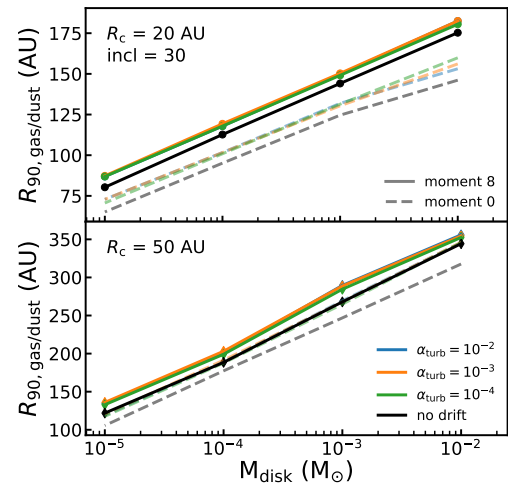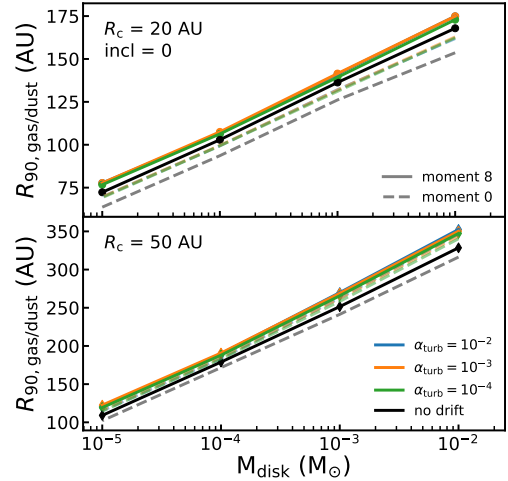Another method would be to measure the gas radius using the peak intensity map, which is the intensity at peak velocity. This map has units identical to the continuum emission (Jy beam^{-1}). Compared to the moment 0 map more weight is placed in the outer parts of the disc, moving $R_{90,gas}$ outwards. By removing the dependence on the line width the peak intensity map might also be less affected by inclination (cf. Appendix A).

Figure C.1 shows a comparison between gas outer radii derived from the moment 0 map (shown on the left) and the

peak intensity map (shown on the right) for three different inclinations. For the inclined discs ($i = 30, 60°$), there is indeed more emission in the outer disc for the peak intensity map. In all cases $R_{90,\text{gas}}$(peak int.) is larger than the $R_{90,\text{gas}}$(mom 0).

In Fig. C.2 $R_{90,\text{gas}}$(peak int.) and $R_{90,\text{gas}}$(mom 0) are compared as functions of disc mass and inclination. Over the mass range examined we find that $R_{90,\text{gas}}$(peak int.) > $R_{90,\text{gas}}$(mom 0). However, apart from this offset, $R_{90,\text{gas}}$(peak int.) follows the same trend with disc mass as $R_{90,\text{gas}}$(mom 0) and is also similarly affected by inclination.

Appendix D: Continuum intensity profiles for $R_c = 20$ AU
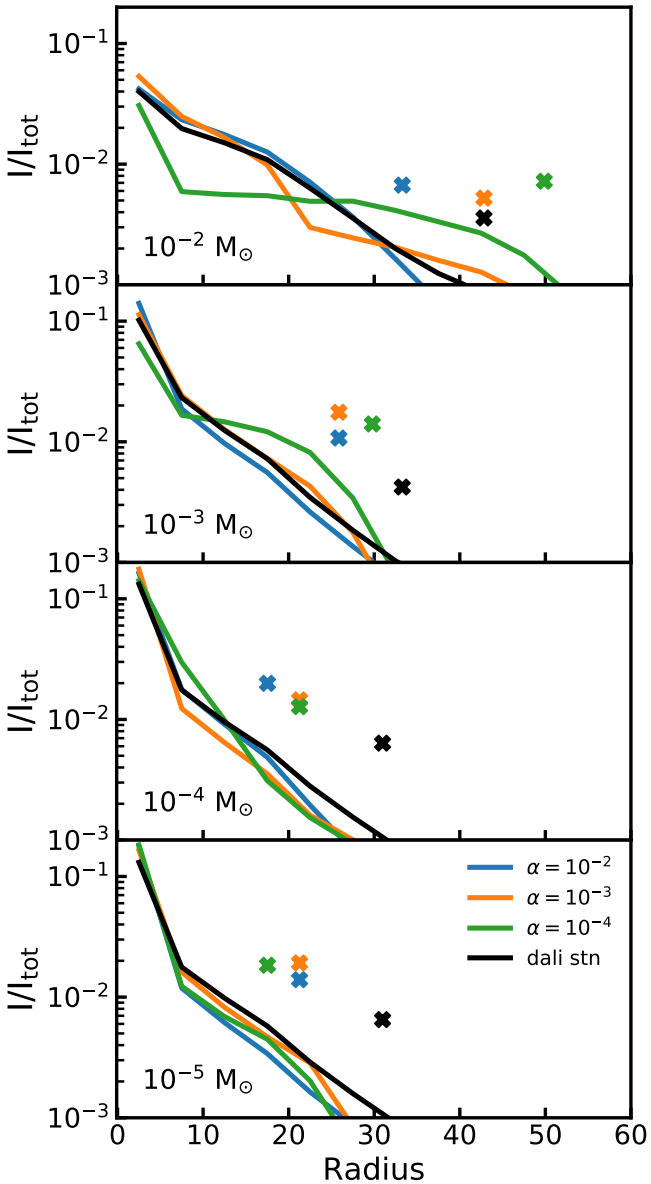
Fig. D.1. Radial profiles of 1300 μm normalised to the total flux. Crosses above the line denote the radii enclosing 90% of the flux (heights of the crosses are arbitrary).

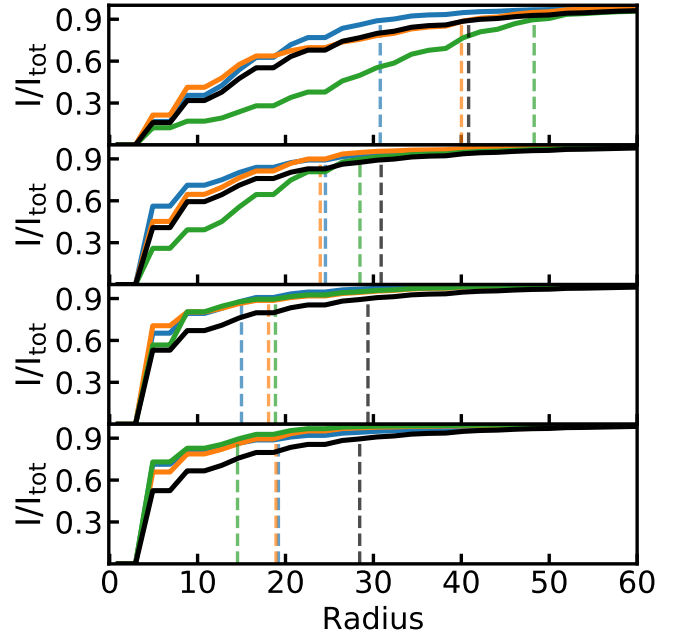**Fig. D.2.** 1300 μm curve of growth of the profiles seen in Fig. D.1. Dashed vertical line denotes the radii enclosing 90% of the flux.

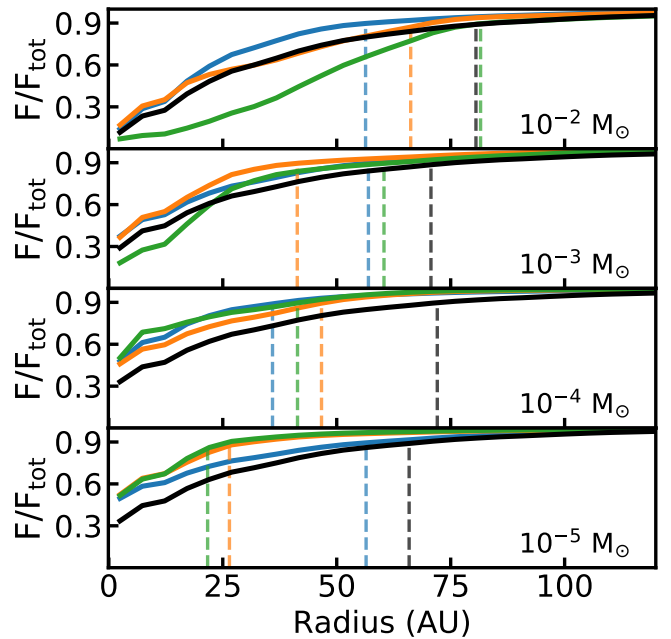## Appendix E: Curves of growth for the $R_c = 50$ AU dust profiles

Fig. E.1. 1300 μm curve of growth of the profiles seen in Fig. 1. Dashed vertical line denote the radii enclosing 90% of the flux.

Appendix F: Deriving a relation between $R_{90,\text{gas}}$ and the CO column density

In Sect. 3.2 the ^{12}CO emission profile was found to quickly drop off at a point very close to where the CO column density (N_{CO}) drops below 10^{15} cm^{-2}. Defining $R_{\text{CO disk}}$ as the radius where $N_{\text{CO}} = 10^{15}$ cm^{-2}, we can derive an analytical relation between $R_{90,\text{gas}}$ and $R_{\text{CO disk}}$.

Using Eq. (3), $R_{90,\text{gas}}$ is defined as

$$0.9 = \frac{2\pi}{F_{\text{tot}}} \int_0^{R_{90,\text{gas}}} I_{\text{CO}}(r')r'\,dr' \tag{F.1}$$

$$= \frac{\int_0^{R_{90,\text{gas}}} I_{\text{CO}}(r')r'\,dr'}{\int_0^{R_{\text{CO disk}}} I_{\text{CO}}(r')r'\,dr'}. \tag{F.2}$$

In this case we used the fact that $R_{\text{CO disk}}$ effectively encloses all of the ^{12}CO flux (cf. Fig. 2). If we assume that the ^{12}CO emission is optically thick, $I_{\text{CO}}(R) = \frac{2\nu^2}{c^2}k_B T(R)$, the equation can be rewritten

$$0.9 = \frac{\int_0^{R_{90,\text{gas}}} T(r')r'\,dr'}{\int_0^{R_{\text{CO disk}}} T(r')r'\,dr'}, \tag{F.3}$$

where T_{gas} is the gas temperature in the CO emitting layer. The temperature profile can often be well described by a power law, $T(R) = T_c(R/R_c)^{-\beta}$, which can be substituted in the integrals

$$0.9 = \frac{\int_0^{R_{90,\text{gas}}} \left(\frac{r'}{R_c}\right)^{-\beta} r'\,dr'}{\int_0^{R_{\text{CO disk}}} \left(\frac{r'}{R_c}\right)^{-\beta} r'\,dr'} \tag{F.4}$$

$$= \frac{\left[\frac{1}{2-\beta}r'^{2-\beta}\right]_0^{R_{90,\text{gas}}}}{\left[\frac{1}{2-\beta}r'^{2-\beta}\right]_0^{R_{\text{CO disk}}}} \tag{F.5}$$

$$= \frac{R_{90,\text{gas}}^{2-\beta}}{R_{\text{CO disk}}^{2-\beta}}, \tag{F.6}$$

where we assumed $0 < \beta < 2$.

We find that $R_{90,\text{gas}}$ and $R_{\text{CO disk}}$ are related through

$$R_{90,\text{gas}} = 0.9^{\frac{1}{2-\beta}} R_{\text{CO disk}} = f^{\frac{1}{2-\beta}} R_{\text{CO disk}}, \tag{F.7}$$

where f represents a more general case where the gas outer radius is defined using a flux fraction f.

Appendix G: Beam size and peak S/N for all disc masses vs. $R_{90,\text{gas}}/R_{90,\text{dust}}$
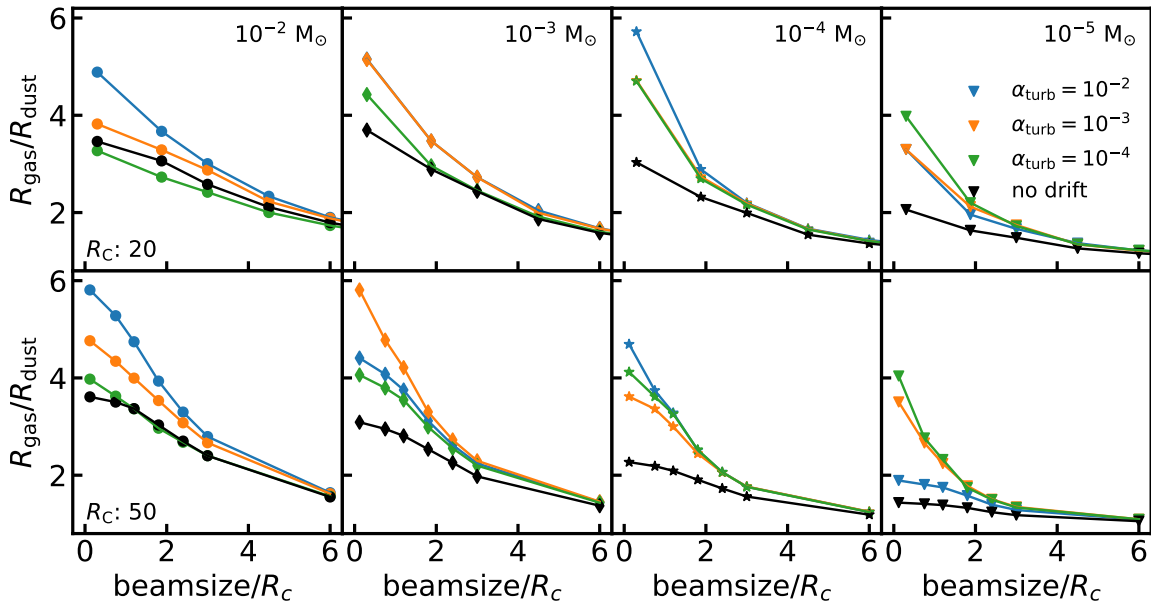

Fig. G.1. Beam size vs. $R_{90,\text{gas}}/R_{90,\text{dust}}$. The effect of the beam scales with its relative size compared to the size of the disc. To highlight this, the beam size is expressed in terms of the characteristic size of the disc.
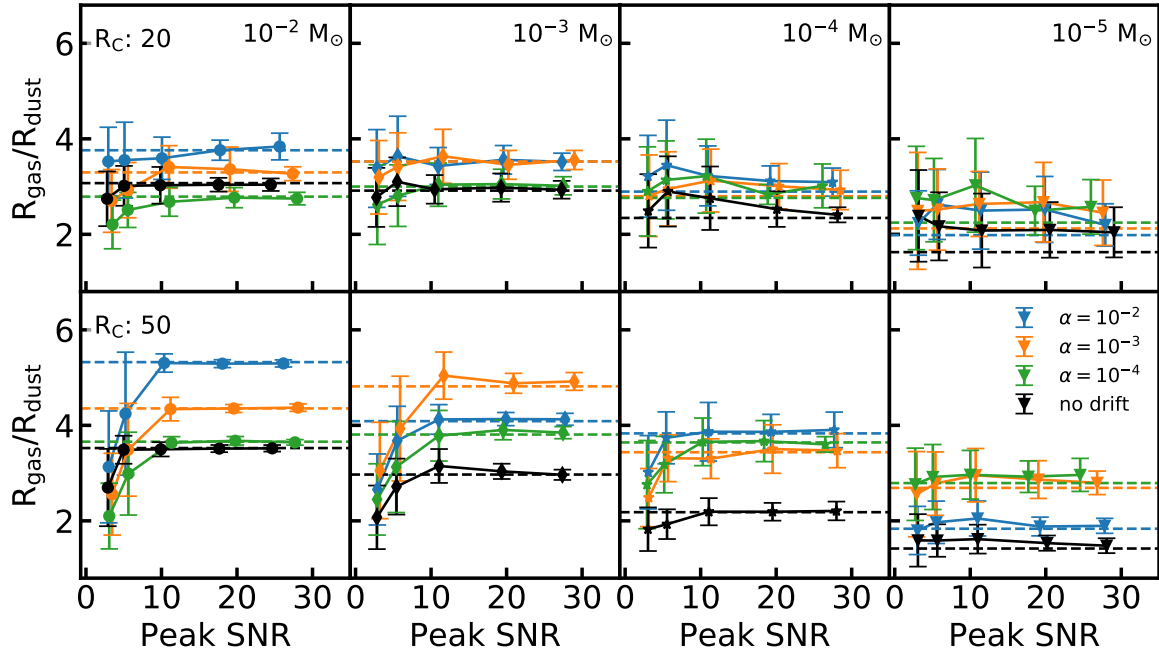
Fig. G.2. Peak S/N in the moment 0 map of the ^{12}CO vs. $R_{90,\text{gas}}/R_{90,\text{dust}}$.

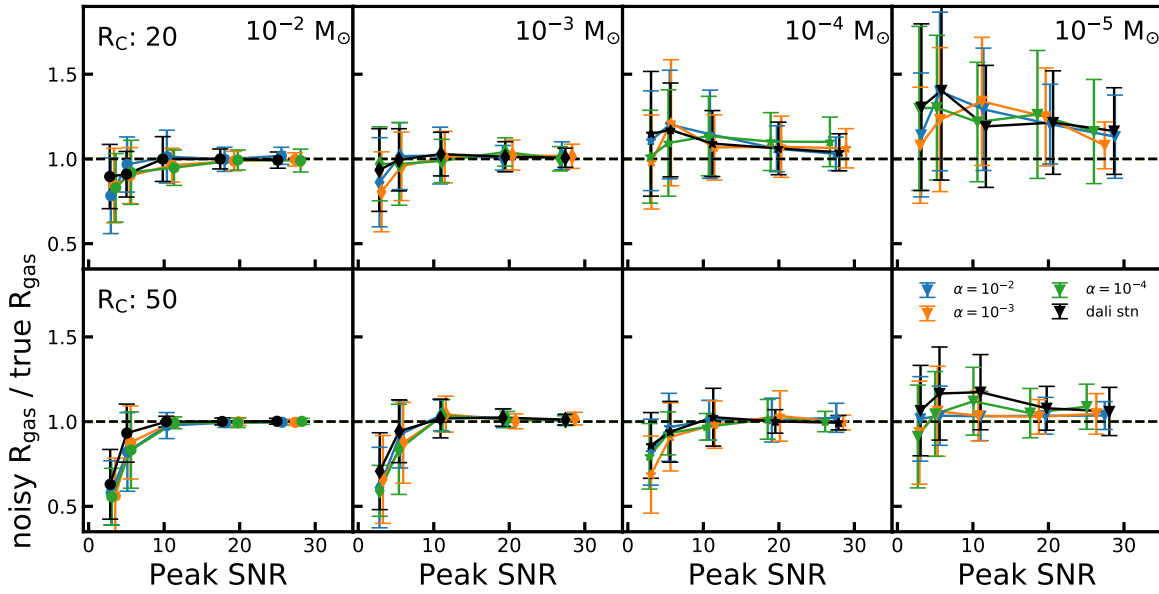## Appendix H: Gas radii vs. peak S/N

Fig. H.1. Peak S/N vs. noisy $R_{90,\text{gas}}$ normalised to the $R_{90,\text{gas}}$ obtained from the noiseless case.

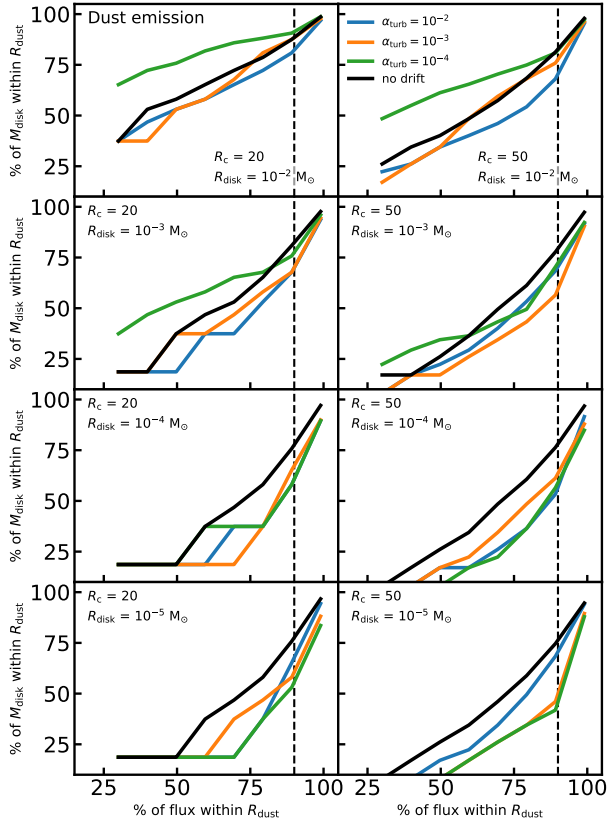## Appendix I: Mass fractions and flux fractions for the remaining discs

Fig. I.1. Fraction of continuum flux used to calculate $R_{90,dust}$ compared to the fraction of M_{disc} within $R_{90,gas}$. Dashed vertical line indicates 90% of the flux.
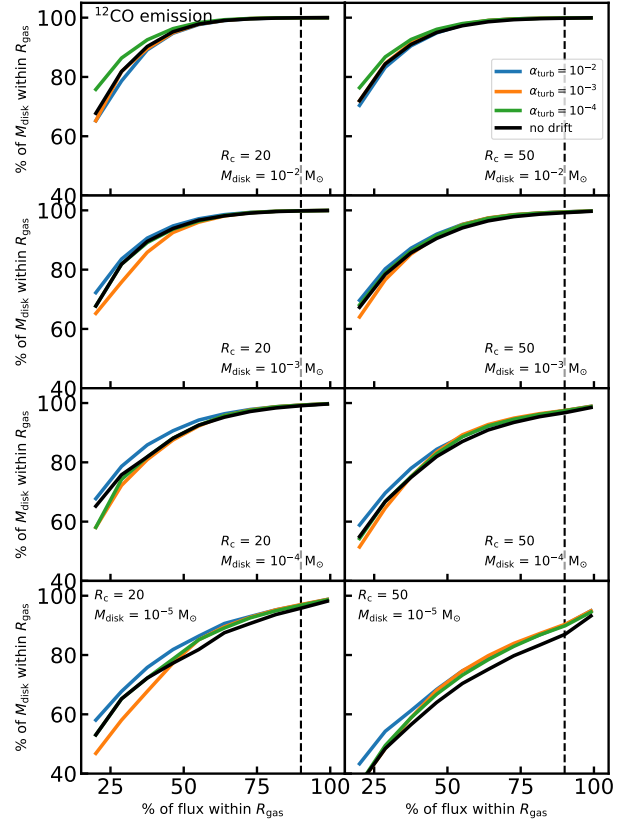
Fig. I.2. Fraction of ^{12}CO flux used to calculate $R_{90,gas}$ compared to the fraction of M_{disc} within $R_{90,gas}$. Dashed vertical line indicates 90% of the flux.